

THE IMPACT OF STAR FORMATION AND FEEDBACK RECIPES ON THE STELLAR MASS AND INTERSTELLAR MEDIUM OF HIGH-REDSHIFT GALAXIES

HARLEY KATZ^{1,2*}, MARTIN P. REY³, CORENTIN CADIOU⁴, TAYSUN KIMM⁵ & OSCAR AGERTZ⁴

¹Department of Astronomy & Astrophysics, University of Chicago, 5640 S Ellis Avenue, Chicago, IL 60637, USA

²Kavli Institute for Cosmological Physics, University of Chicago, Chicago IL 60637, USA

³Sub-department of Astrophysics, University of Oxford, Keble Road, Oxford OX1 3RH, United Kingdom

⁴Lund Observatory, Division of Astrophysics, Department of Physics, Lund University, Box 43, SE-221 00 Lund, Sweden and

⁵Department of Astronomy, Yonsei University, 50 Yonsei-ro, Seodaemun-gu, Seoul 03722, Republic of Korea

Version February 2, 2026

ABSTRACT

We introduce MEGATRON, a new galaxy formation model for cosmological radiation hydrodynamics simulations of high-redshift galaxies. The model accounts for the non-equilibrium chemistry and heating/cooling processes of ≥ 80 atoms, ions, and molecules, coupled to on-the-fly radiation transfer. We apply the model in a cosmological setting to the formation of a $10^9 M_{\odot}$ halo at $z = 6$, and run 25 realizations at pc-scale resolution, varying numerous parameters associated with our state-of-the-art star formation, stellar feedback, and chemical enrichment models. We show that the overall budget of feedback energy is the key parameter that controls star formation regulation at high redshift, with other numerical parameters (e.g. supernova clustering, star formation conditions) having a more limited impact. As a similar feedback model has been shown to produce realistic $z = 0$ galaxies, our work demonstrates that calibration at $z = 0$ does not guarantee strong regulation of star formation at high-redshift. Interestingly, we find that subgrid model variations that have little impact on the final $z = 6$ stellar mass can lead to substantial changes on the observable properties of high-redshift galaxies. For example, different star formation models based on, e.g. density thresholds or turbulence inspired criteria, lead to fundamentally distinct nebular emission line ratios across the interstellar medium (ISM). These results highlight the ISM as an important resource for constraining models of star formation, feedback, and galaxy formation in the JWST era, where emission line measurements for $> 1,000$ high-redshift galaxies are now available.

Subject headings: high-redshift galaxies, ISM, galaxy formation

1. INTRODUCTION

The launch of JWST (Gardner et al. 2006, 2023) has ushered in a new era for high-redshift galaxy formation. The spectroscopic redshift barrier set by HST at $z \sim 11$ (Oesch et al. 2016) has been far surpassed (e.g. Curtis-Lake et al. 2023; Wang et al. 2023; Carniani et al. 2024), while emission lines that provide detailed insight into the ISM have been detected to $z > 12$ (Zavala et al. 2024; Castellano et al. 2024).

This new data immediately challenged conventional understanding of galaxy formation in the early Universe. For example, numerous high-redshift galaxy surveys with JWST have reported the detection of an overabundance of bright galaxies at $z \gtrsim 9$ compared to earlier constraints from Hubble and most theoretical models (e.g. Finkelstein et al. 2023b; Harikane et al. 2024; Leung et al. 2023; Chemerynska et al. 2023, although c.f. Willott et al. 2023). Likewise, massive quiescent galaxies at $z \sim 3 - 5$ appear to form at exceptionally early epochs (e.g. de Graaff et al. 2024; Glazebrook et al. 2024). Many early galaxies exhibit chemical abundance patterns that have never been seen in the gas-phase (e.g. Cameron et al. 2023a; Senchyna et al. 2024; Isobe et al. 2023b; Topping et al. 2024b), which may indicate exotic enrichment channels, e.g. from supermassive stars (e.g. Charbonnel et al. 2023; Marques-Chaves et al. 2024). Moreover the ISM gas temperatures in early galaxies may be at odds with

standard heating mechanisms (e.g. Katz et al. 2023c; Laseter et al. 2024). Finally, some of the high-redshift JWST spectra appear to require exotic stellar populations or a top-heavy stellar initial mass function (e.g. Cameron et al. 2023b; Katz et al. 2024a).

These new anomalies supplement a previous set of inconsistencies between simulations and observations that arose from HST/ALMA data including the presence of high-redshift Balmer breaks (Hashimoto et al. 2018), extremely high [O III] $88 \mu\text{m}$ /[C II] $158 \mu\text{m}$ ratios (Harikane et al. 2020), or very extended cold gas haloes (Fujimoto et al. 2020).

Understanding the physical mechanisms responsible for the discrepancies between simulations and observations remains a key theoretical challenge. For example, numerous solutions to the overabundance of bright galaxies have been proposed including changes to the star formation efficiency (e.g. Dekel et al. 2023; Feldmann et al. 2025), the absence of dust (Ferrara, Pallottini & Dayal 2023), M_{UV} variability (e.g. Mason, Trenti & Treu 2023; Shen et al. 2023; Sun et al. 2023; Kravtsov & Belokurov 2024), IMF variations (e.g. Yung et al. 2024), chemical anomalies (Katz et al. 2024b), or nebular emission (Katz et al. 2024a).

Prior to JWST, numerous numerical simulations of the early Universe such as AURORA (Pawlik et al. 2017), CoDa (Ocvirk et al. 2020), CROC (Gnedin 2014), FIRE (Ma et al. 2018), FIREbox HR (Feldmann et al. 2025), FirstLight (Ceverino, Glover & Klessen 2017), (Ma et al.

*E-mail: harleykatz@uchicago.edu

2018), FLARES (Lovell et al. 2021), OBELISK (Trebitsch et al. 2021), RENAISSANCE (O’Shea et al. 2015), SERRA (Pallottini et al. 2022), SPHINX (Rosdahl et al. 2018), and THESAN (Kannan et al. 2022) were very successful in reproducing observational data such as the UV luminosity function, despite fundamental differences in resolution (spatial and mass), subgrid models for star formation, feedback, and metal enrichment, and included physics such as radiative transfer, non-equilibrium cooling, and dust. This demonstrates that the constraining power of the UV luminosity function is rather limited.

Part of the reason why UV luminosity has poor constraining power is that it is generally only sensitive to the younger stellar populations in the galaxy (e.g. Kennicutt & Evans 2012) rather than the full star formation history. For this reason, the inferred stellar mass-halo mass relation (e.g. Moster, Naab & White 2018; Behroozi et al. 2019) has been a common benchmark. However, neither stellar mass nor halo mass are directly observable quantities, rather they are inferred from observations under a set of assumptions that may differ from those used in models. This can lead to systematic errors in comparing inferred and modeled stellar mass-halo mass relations. Furthermore, no pre-JWST simulation reliably predicted the stellar mass function in the interval $z \sim 4 - 9$ (Weibel et al. 2024). Stellar mass in particular has order of magnitude uncertainties depending on choice of prior of star formation history (Narayanan et al. 2024) and this manifests in studies that observe galaxies with similar redshifts and fluxes predicting vastly different stellar masses (Katz et al. 2023b). Convergence also has not yet been reached in studies comparing spatially resolved and integrated stellar masses (Giménez-Arteaga et al. 2023, 2024). Most importantly, the models used to infer the stellar mass-halo mass relation are inconsistent with the new high-redshift JWST data (Finkelstein et al. 2023b). Because JWST can see much redder than HST, rather than using inferred stellar masses, constraints on the older stellar populations are available via photometry (and/or spectra), if they can be forward modeled.

In addition to observing older stellar populations at longer wavelengths, another advantage of JWST is the ability to probe into the ISM of early galaxies for large samples (e.g. Cameron et al. 2023c; Sanders et al. 2023), which complements what can be done with ALMA for much fewer numbers of galaxies (e.g. Carniani et al. 2025; Schouws et al. 2025). These studies have demonstrated that the nebular conditions in the early Universe are vastly different compared to those in local galaxies. Comparing simulations with the observed ISM conditions at high redshift via rest-frame UV and optical emission lines represents a new opportunity to test the physics present in numerical simulations.

However, among the larger-scale simulation suites, only a few projects such as FIRE, FIREBox HR, Obelisk, SERRA, SPHINX, and RENAISSANCE have the resolution to begin to probe the ISM (at the cost of modeling either a smaller volume, fewer galaxies, or stopping the simulation at high-redshift). Such simulations often use more simplistic models than what is considered the state-of-the-art in the ISM simulation community (Kim et al. 2023). Simulations with detailed ISM models are often limited to either isolated or small high-redshift dwarf galaxies (e.g. Safranké-Shrader, Milosavljević & Bromm 2014a; Hu et al. 2016; Steinwandel et al. 2020; Hislop et al. 2022; Katz et al. 2022; Deng et al. 2024b), which limits the possible comparison between the models and JWST observations. Moreover, much of the detailed information from JWST comes in the form of emission lines from both primordial species (e.g. H α , H β , He II λ 1640) and metals (e.g. [O III] λ 5007, [O II] λ 3727, [C III] λ 1908), many of which are not self-consistently predicted by the current generation of simulations.

Predicting emission lines (and more generally the full spectra of galaxies) requires knowing the detailed properties of the radiation field and thermodynamics of both ionized and neutral gas. Cosmological radiation hydrodynamics codes often include non-equilibrium chemistry for primordial species (e.g. Pawlik & Schaye 2008; Rosdahl et al. 2013; Gnedin 2014), but few include non-equilibrium metal chemistry, the effects of which have recently been shown to be important for some emission lines (e.g. Richings et al. 2022; Katz et al. 2022). Resolving the detailed structure of the H II regions is also crucial (e.g. Jin, Kewley & Sutherland 2022) and this remains well beyond the capabilities of current simulations of full galaxies. Nevertheless, in order to take advantage of the most recent JWST data as a means of both understanding the physics that governs our own Universe and for constraining theoretical models of galaxy formation, detailed galaxy-scale models of the ISM are required to forward-model the observations.

For this reason, in this work we adopt the RAMSES-RTZ code (Katz 2022) to distill the physics from numerics of early galaxy formation. RAMSES-RTZ is unique among galaxy formation codes as it not only solves for gravity, hydrodynamics, radiation transfer, and primordial chemistry, but it can also follow the non-equilibrium chemistry of metals, fully coupled to the radiative transfer, which is the key component for predicting emission lines. The large chemical network drastically increases the number of emission lines that can be predicted in a non-equilibrium manner compared to previous generations of simulations (e.g. Lupi et al. 2020). We develop a new, state-of-the-art galaxy formation model and systematically test how modifications to sub-grid parameters, feedback physics, and resolution, impact the stellar mass growth and the ISM of a single high-redshift dwarf galaxy. We demonstrate how the ISM, in particular observable emission line ratios, exhibit strong sensitivity to subtle changes in subgrid recipes and feedback, and thus represent a new means of constraining models of galaxy formation.

2. METHODS

In this work, we describe a new model for high-redshift galaxy formation: MEGATRON. The model is developed as part of the RAMSES-RTZ code (Katz 2022), based on RAMSES (Teyssier 2002) and RAMSES-RT (Rosdahl et al. 2013; Rosdahl & Teyssier 2015). In this section, we outline our fiducial model and a broad parameter study of subgrid physics and numerical resolution.

2.1. Gravity & Hydrodynamics

We numerically solve the equation of hydrodynamics in the simulation with a closure between gas pressure and internal energy with an adiabatic index of $\gamma = 5/3$, suited for an ideal monoatomic gas. The associated non-linear conservation laws are evolved with a MUSCL-Hancock scheme (van Leer 1979) using a linear reconstruction of the conservative variables at cell interfaces with a MinMod total variation diminishing scheme, and using the HLLC approximate Riemann solver (Toro 2009). We use a Courant factor of 0.8. Dynamics of collisionless star and dark matter (DM) particles are computed using a particle-mesh solver and we compute their contribution to the gravitational potential using cloud-in-cell interpolation. Gravitational accelerations are calculated using a finite-difference of the potential; the latter is computed from the total density $\rho = \rho_{\text{gas}} + \rho_{\star} + \rho_{\text{DM}}$ using a multigrid scheme (Guillet & Teyssier 2011).

2.2. Chemistry & Thermodynamics

Our model is unique among large cosmological simulations in that it employs the PRISM model (Katz et al. 2022), which includes a large non-equilibrium thermochemistry network for primordial species, metals, and molecules that are

fully coupled to on-the-fly multi-frequency radiation transfer. Compared to previous studies, improved modeling of the gas thermochemistry allows us to more accurately predict the non-equilibrium emission and absorption from the ISM and CGM.

2.2.1. Chemical Model

In total we consider 82 species for our non-equilibrium calculation:

- **Primordial species:** H I-II, He I-III, e^- ,
- **Metal ions:** C I-VI, N I-VII, O I-VIII, Ne I-X, Mg I-X, Si I-XI, S I-XI, & Fe I-XI,
- **Molecules:** H_2 & CO.

While RAMSES-RTZ is capable of handling all ionization states of each metal ion, we have restricted ourselves to what we define as the “minimal cooling model”. Using CLOUDY (Ferland et al. 2017), we calculate the contribution of each metal ion to the total equilibrium cooling rate in the temperature range $10 - 10^9$ K under the assumption of a Haardt & Madau (2012) UV background at $z = 2$. We only model in non-equilibrium those ions that contribute at least 1% to the total equilibrium cooling rate across the aforementioned temperature range. This decreases by 40% the number of metal ions to be followed out-of-equilibrium, easing the memory requirements to adapt our model to modern supercomputers. All ions that are not followed in non-equilibrium are still considered under the assumption of collisional ionization equilibrium.

The non-equilibrium evolution of the aforementioned species are modelled as described in Katz (2022); Katz et al. (2022). More specifically, we account for ionization, recombination, and charge exchange processes. For H and He, collisional ionization and radiative and dielectronic recombination are adopted following Rosdahl et al. (2013) based on rates from Cen (1992) and Hui & Gnedin (1997), respectively. Radiative and dielectronic recombination recombination rates for metals are largely taken from Badnell (2006) and Badnell et al. (2003), respectively, with the exception of certain higher ionization states¹ of heavy elements where we rely on Aldrovandi & Pequignot (1973); Shull & van Steenberg (1982); Arnaud & Rothenflug (1985); Arnaud & Raymond (1992). Collisional ionization rate fitting functions for metals are adopted from Voronov (1997). Charge exchange reaction rates are compiled from Kingdon & Ferland (1996); Stancil et al. (1999); Barragán et al. (2006). Recombination on the surface of dust grains is computed using reaction rates taken from Weingartner & Draine (2001). All atoms and their ions are subject to photoionization. Cross sections for all atomic species and their ions are calculated using the analytic fits from Verner et al. (1996). Although the PRISM model can also handle ionization from cosmic-rays, for this work, we neglect their effects, as they will be considered in future work using a fully-coupled CR solver (e.g. Rodríguez Montero et al. 2024).

The formation and destruction of H_2 and CO molecules is described in Katz et al. (2017, 2022). H_2 formation proceeds via two channels: primordial reactions stimulated by H^- and formation on dust. Primordial rates follow those presented in Glover et al. (2010) while dust formation rates are a combination of Gnedin, Tassis & Kravtsov (2009) and Bialy & Sternberg (2019) (see Katz et al. 2022). Due to finite spatial resolution, we artificially enhance the formation rate of H_2 by a factor of 10 (see also Gnedin, Tassis & Kravtsov 2009)

¹ We rely on Badnell et al. (2003); Badnell (2006) where possible. If the species is not available in those datasets, we revert to older data.

to account for unresolved, sub-grid clumping. Note that such small-scale clumping is expected to occur below the grid scale (which is a $\sim 1 - 20$ pc for the simulations presented here) due to unresolved turbulence that typically leads to a log-normal gas density probability distribution function. Destruction of H_2 can occur through collisions or via photodissociation (direct and via recombinative dissociation). Collisional dissociation rates are adopted from Glover & Abel (2008) while cross-sections in the Lyman-Werner and ionizing bands are as described in Baczynski, Glover & Klessen (2015). We include H_2 self-shielding at outlined Katz et al. (2017).

CO formation and destruction is based on Nelson & Langer (1997); Glover & Clark (2012) with modifications as described in Katz et al. (2022). The physical mechanism of CO formation is assumed to be initiated by H_2 and C^+ which goes on to form CH_x molecules. The rate limiting steps are then dictated by the survivability of CH_x molecules. Destruction of CO and CH_x molecules are assumed to be dominated by far UV radiation with destruction rates adopted from Heays, Bosman & van Dishoeck (2017). We note that, in principle, the formation rate of CO is subject to the same sub-grid clumping as assumed for H_2 . However, since H_2 is the primary reactant in the formation of CO, our subgrid clumping factor also propagates into the formation of CO. In previous work, we focused on the ISM and thus neglected collisional destruction of CO since photodissociation by UV radiation is the dominant process in such environments. In this work, we supplemented the model to account for collisional destruction of CO by electrons in high-temperature gas. This provides a destruction path for CO ejected from the galaxy in a wind, where the radiation field is weak and the temperature is high².

Much of the chemistry described above relies on knowing the dust content in each gas cell in the simulation. We employ an empirical model where the dust-to-gas mass ratio is assumed to follow a broken power-law as a function of metallicity following observations of the local Universe (Rémy-Ruyer et al. 2014). To remain consistent with these observations, the composition of the dust is that of the BARE-GR-S model of Zubko, Dwek & Arendt (2004). We assume that dust is only present in cells with $T < 10^6$ K and use the chemical composition of the BARE-GR-S dust model to self-consistently compute the depletion factors of each metal into the dust phase. As described in Katz et al. (2022), because elements are enriched individually, metal abundance ratios can significantly deviate from solar abundance patterns. To avoid unphysical depletion rates, we cap the maximum depletion rate of each metal to those at solar metallicity defined in Dopita et al. (2000); Grevesse et al. (2010). Future work will self-consistently couple dust grains to the thermochemistry (Rodríguez-Montero et al. *in prep.*).

2.2.2. Heating & Cooling

PRISM has been designed to reproduce the expected equilibrium of the local ISM (e.g. Wolfire et al. 1995, 2003) but generalized into a 3D non-equilibrium galaxy formation setting (see Figure 1 of Katz et al. 2022). Our approach is here fundamentally different from other large simulations, where radiative heating and cooling is often determined by combining a UV background and CLOUDY tables (e.g. Schaye et al. 2015; Pillepich et al. 2018; Dubois et al. 2014; Feldmann et al. 2023). This is motivated by the fact that, in 1D tests, such models often fail to reproduce the equilibrium pressure-density relation observed in the local ISM (Kim et al. 2023).

² More specifically, we adopt the UMIST rate (McElroy et al. 2013) for $CO^+ + e^- \rightarrow C + O$. This rate naively over-predicts the destruction mechanism that we are interested in due to the additional Coulomb attraction and thus we exponentially suppress the rate below temperatures of 2×10^5 K.

Note that a subset of simulations have attempted to account for either the local radiation field or non-equilibrium effects in the context of cosmological simulations (e.g. [Gnedin & Hollon 2012](#); [Oppenheimer et al. 2018](#); [Capelo et al. 2018](#); [Lupi et al. 2020](#)); however, the models are either specifically designed for the warm and cold ISM, ignore the local radiation field, do not track higher ionization states of metals that matter for the CGM or ionized gas more generally, or do not follow the impact of individual elements on the cooling function.

Our full heating and cooling model is nearly identical to that presented in [Katz et al. \(2022\)](#). It includes photoheating ([Rosdahl et al. 2013](#)), photoelectric heating ([Bakes & Tielens 1994](#); [Wolfire et al. 1995, 2003](#)) with corrections due to a different assumed PAH abundance ([Zubko, Dwek & Arendt 2004](#)), and heating from H_2 formation ([Sternberg & Dalgarno 1989](#); [Röllig et al. 2006](#)) and H_2 excitation/dissociation ([Black & Dalgarno 1977](#); [Draine & Bertoldi 1996](#); [Burton, Hollenbach & Tielens 1990](#)).

We account for cooling from primordial species ([Cen 1992](#); [Hui & Gnedin 1997](#); [Rosdahl et al. 2013](#); [Osterbrock & Ferland 2006](#); [Haiman, Thoul & Loeb 1996](#); [Black 1981](#)), H_2 ([Moseley et al. 2021](#)), CO ([McKee et al. 1982](#); [Hollenbach & McKee 1989](#); [Koyama & Inutsuka 2000](#)), dust recombination ([Wolfire et al. 2003](#)), dust-gas collisional processes ([Hollenbach & McKee 1989](#); [Draine 2011](#); [Bialy & Sternberg 2019](#)), and metal lines. At $T < 10^4$ K, cooling from metal lines is calculated for C I, C II, N II, O I, O III, Ne II, Si I, Si II, S I, Fe I, and Fe II, under the approximation of a two- or three-level ion as appropriate. We consider the following collisional partners: H, H^+ , ortho and para H_2 , e^- , He, He^+ , and He^{++} , with collision rates adopted from [Ferland et al. \(2017\)](#). At $T > 10^3$ K, we have created tables of cooling rates from CLOUDY ([Ferland et al. 2017](#)) that are interpolated ion-by-ion assuming that electrons are the only collisional partner. In the regime $10^3 \leq T/\text{K} \leq 10^4$, we subtract the cooling contribution from the ions that we compute explicitly from the cooling tables to prevent double counting. At $T \sim 10^4$ K, we smoothly interpolate between the explicit computation and the cooling tables using the method presented in [Bovino et al. \(2016\)](#). We assume collisional ionization equilibrium (CIE) for ions that are followed in equilibrium, and we interpolate our cooling tables to account for their impact on the gas thermochemistry (e.g. [Gray, Scannapieco & Kasen 2015](#)).

All chemical reactions, temperature, and photon group (see [Table 1](#)) updates are evolved using a semi-implicit method originally based on [Anninos et al. \(1997\)](#). We adapt the timestep following a 10% rule (e.g. [Rosdahl et al. 2013](#)) so that no quantity changes by more than 10% in each cooling subcycle. This method has been shown to reproduce the behaviour of more complex implicit solvers at a much reduced computational cost ([Katz 2022](#)).

Note that the only major change³ in cooling from [Katz et al. \(2022\)](#) is the extension of the cooling tables below 10^4 K. This change has little impact on the equilibrium pressure-density curve at solar ISM conditions because the cooling is completely dominated by [C II] and [O I] lines for which the new computation is identical. This can be seen in [Figure 1](#) where we show the equilibrium temperature-density (top) and pressure-density (bottom) relations as a function of metallicity comparing the updates applied in this work (solid lines) to that from [Katz et al. \(2022\)](#) (dashed lines). Almost no difference is seen between the models and both agree with observational constraints at solar metallicity because this test predominantly probes the physics of neutral gas.

³ Other minor changes include updating the H_2 cooling function from [Hollenbach & McKee \(1979\)](#); [Galli & Palla \(1998\)](#) to [Moseley et al. \(2021\)](#) and fixing a bug in our dust recombination cooling where a factor of 0.5 was inadvertently missing.

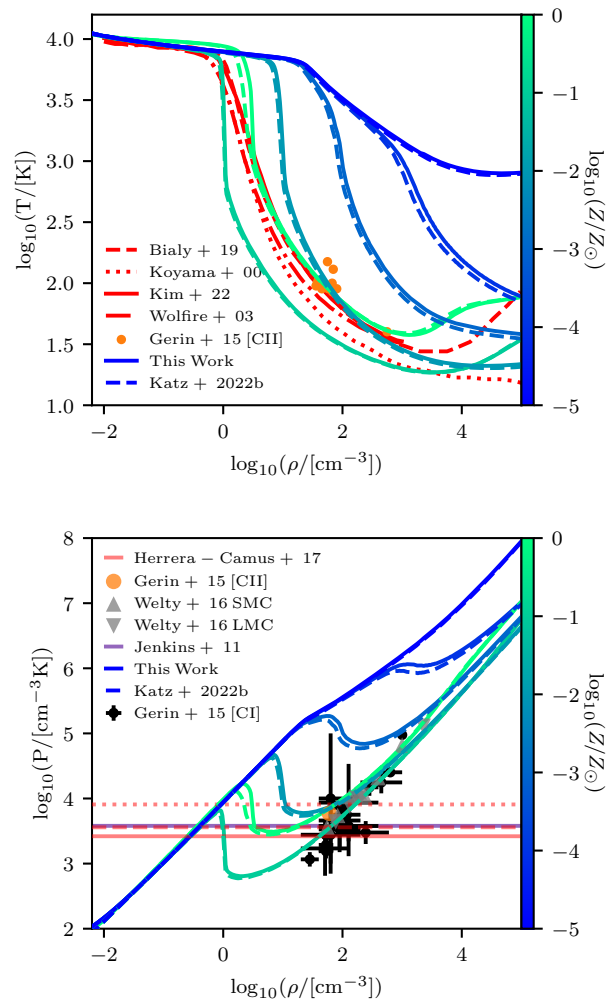


FIG. 1.— (Top) Equilibrium temperature-density (top) and pressure-density (bottom) relations for the thermodynamic model used in MEGATRON, as a function of metallicity (solid lines). For all models, we assume a local ISM radiation field such that $G_0 = 1$ and a background cosmic ray hydrogen ionization rate of 10^{-16} s^{-1} . At solar metallicities (green), the thermodynamic model is consistent with other ISM models ([Bialy & Sternberg 2019](#)), [Koyama & Inutsuka \(2000\)](#), [Kim et al. \(2023\)](#); red dashed, dotted, and solid, respectively) and data in the Milky Way and the LMC/SMC ([Gerin et al. \(2015\)](#), ([Jenkins & Tripp 2011](#)), [Herrera-Camus et al. \(2017\)](#), [Welty et al. \(2016\)](#)); orange points, purple line, red dashed, solid, dotted lines for cold-neutral fractions of 0.7, 0.5, and 0.3, and grey triangles, respectively). Changes in atomic data and reaction rates lead to small variations with the earlier version of the model ([Katz et al. 2022](#), dashed blue lines).

Rather, the extension of the tables results in more accurate cooling in metal-enriched ionized regions where significant cooling contributions from more highly-excited energy levels and ions may be important⁴. To demonstrate the accu-

⁴ For example, in an example solar-metallicity CLOUDY model where the ionized gas temperature is $\sim 8,000$ K in the center of the nebula, ions such as S IV, S III, Ne III, N III, Ar III, Fe III, O II, S II, N II, Mg II, and others all contribute more than 1% of the total cooling rate at some radius in the nebula and hence are likely important for the ionized gas temperature. For this reason, our new cooling model now better captures these ions at $T < 10^4$ K. Note that depletion onto dust and dust model can significantly impact which ions are important and this is self-consistently computed in the MEGATRON model.

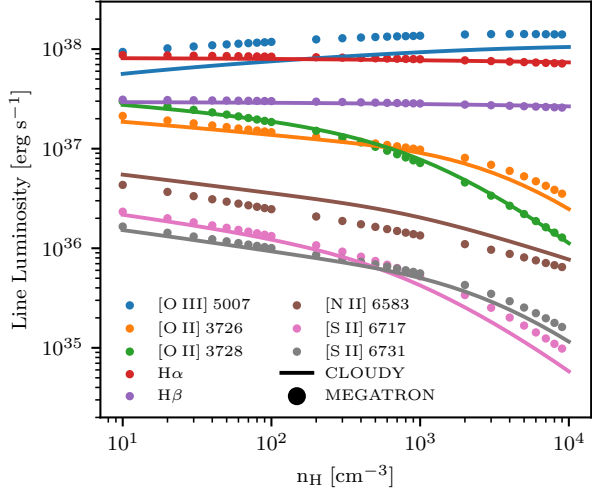


FIG. 2.— Emission line luminosities from a Strömgren sphere around an O4V star in gas with varying density at $0.1 Z_{\odot}$ metallicity. Results from the MEGATRON non-equilibrium, radiative transfer calculation (points) show good agreement with CLOUDY calculations (lines).

racy of the updated model, we have run a series of Strömgren sphere tests where we place a single O4V star modelled as having a blackbody temperature of $42,900 \text{ K}^5$ (Pecaut & Mamajek 2013) at the corner of a uniform density cube of gas initialized at 100 K and $0.1 Z_{\odot}$ metallicity and evolve the radiation field and thermochemistry of the gas until the system reaches equilibrium. Note that hydrodynamics and gravity is excluded from this experiment. We then calculate the emission line luminosities for various strong lines and compare the results to a similar 1D simulation with CLOUDY. In Figure 2, we compare the results from our model (points) with those from CLOUDY (lines). For nearly all lines, the predicted emission line luminosities are in very good agreement. Subtle differences are present for a few reasons. First, we have adopted the default atomic data in PyNeB (Luridiana, Morisset & Shaw 2015) which can differ from CLOUDY. Second, the dust prescription in CLOUDY is different from our model, which has an impact on temperature. We have specifically adopted $0.1 Z_{\odot}$ for this experiment so that dust has an impact on the results but does not necessarily dominate. This has a noticeable effect on the [O III] $\lambda 5007$ line as the gas inside the H II region in our model is slightly hotter than in CLOUDY. Due to the exponential scaling of the emissivity curve for collisionally excited lines, small changes in temperature can lead to significant changes in luminosity. $H\alpha$ and $H\beta$ are much less sensitive to temperature which is why we find such good agreement in the ionized region. Third, we have adopted slightly different values for depletion onto dust in our model than the default in CLOUDY. This has the strongest impact on the nitrogen emission lines where our adopted depletion value is higher. The magnitude of the difference we observe in our code compared to CLOUDY is similar to the differences between CLOUDY and MAPPINGS (D’Agostino et al. 2019)⁶. Hence, we are confident that our model is well-calibrated in both neutral and ionized regimes.

⁵ Stellar parameters for this star can be found at https://www.pas.rochester.edu/~emamajek/EEM_dwarf_UBVIJHK_colors_Teff.txt.

⁶ Across all emission lines in Figure 2, we find a median difference of 0.035 dex between our code and CLOUDY with a maximum difference of 0.22 dex. For comparison, D’Agostino et al. (2019) found a 0.1 dex difference between CLOUDY and MAPPINGS for the BPT diagram.

2.3. Refinement Strategy

We use an adaptive mesh refinement strategy to split grid cells and increase the dynamic range of the simulation. In our fiducial model, refinement is allowed down to 76 pc , constant in comoving units. In other words, the maximum spatial resolution of the simulation slowly degrades with time, going from 3.6 pc at $z = 20$ to 11 pc at $z = 6$. This avoids both numerical effects of releasing grid levels at specified times (e.g. Snaith et al. 2018), and also affords higher spatial resolution at high-redshifts when haloes are much smaller in mass and radius. We combine a quasi-Lagrangian refinement strategy with additional super-Lagrangian refinement criteria targeting the Jeans’ length. A cell is flagged for refinement into 8 equally-sized children cells if

1. either the cell mass exceeds $M_{\text{DM,cell}} + \frac{\Omega_m}{\Omega_b} M_{\text{b,cell}} > 8 m_{\text{DM}}$, where $M_{\text{DM,cell}}$ and $M_{\text{b,cell}}$ are respectively the DM and baryon (stars + gas) mass in the current cell,
2. or the cell size is at least a quarter of the local Jeans length

$$\lambda_J = \sqrt{\frac{\pi c_s^2}{G\rho}}, \quad (1)$$

where $c_s = \sqrt{\gamma k_b T / m_p}$ is the sound speed, G is the gravitational constant, ρ is the gas density and m_p is the proton mass,

3. and the value of the passive scalar (that identifies cells in the Lagrange volume) in the cell is larger than 0.9^7 .

When refining cells, we directly inject the conservative variables (density, momentum, etc.) into the children cells.

We use adaptive time stepping, where the time step is halved wherever resolution is doubled. In the following, we will refer to the ‘fine’ time step as the shortest time step, and as the ‘coarse’ time step as the time step of the base grid (39 kpc comoving).

2.4. Star Formation

Once the gas has cooled and condensed sufficiently, we consider several approaches to spawning star particles in the simulation.

2.4.1. Turbulence Inspired Star Formation

Our fiducial algorithm assumes that star formation occurs in the simulation based on estimates of the local turbulent properties of the gas (Kimm et al. 2017). The algorithm is inspired by high-resolution simulations of turbulent star forming gas clouds (e.g. Padoan & Nordlund 2011; Federrath & Klessen 2012). The method is identical to that presented in Rosdahl et al. (2018) and similar to what was used in Agertz et al. (2021).

We consider a gas cell eligible for star formation if it satisfies the following criteria:

1. The gas density is $> 10 \text{ cm}^{-3}$ and $> 200\times$ the mean background. The former threshold has negligible impact on the simulation and is set purely for computational efficiency while the latter is designed so that stars do not form outside haloes at unrealistically high redshifts.
2. The turbulent Jeans length (see Equation 2 of Rosdahl et al. 2018 or alternatively Bonazzola et al. 1987; Federrath & Klessen 2012) is smaller than the cell size (i.e. unresolved).

⁷ When we create the initial conditions of the zoom simulation, all cells that are on the maximum level of refinement are tagged with a passive scalar of 1, while all other cells have this value set to 0. This passive scalar follows gas flows, allowing us to easily identify where the Lagrange region is throughout the simulation.

3. The gas cell is a local density maximum compared to the six neighbouring cells.
4. The gas flow is locally converging (as measured from the six neighbouring cells).

When a gas cell is flagged for star formation the star formation rate density is computed as

$$\dot{\rho}_* = \epsilon_* \frac{\rho}{t_{\text{ff}}}, \quad (2)$$

where ρ is the gas density of the cell, t_{ff} is the gas free-fall time, and ϵ_* is the efficiency by which the gas is converted into stars over a free-fall time. The efficiency is estimated again from the local turbulent gas properties such that

$$\epsilon_* = \frac{\epsilon_{\text{acc}}}{2\phi_t} \exp\left(\frac{3}{8}\sigma_s^2\right) \left[1 + \text{erf}\left(\frac{\sigma_s^2 - s_{\text{crit}}}{\sqrt{2}\sigma_s^2}\right)\right], \quad (3)$$

where $\epsilon_{\text{acc}} = 0.5$ is the accretion fraction of gas onto stars, $1/\phi_t = 0.57$, $\sigma_s^2 = \ln(1 + b^2 \mathcal{M}^2)$, $b = 0.4$ (which assumes a mixture of compressive and solenoidal modes), \mathcal{M} is the Mach number (see also Padoan & Nordlund 2011; Federrath & Klessen 2012) which is computed from the local properties of the gas. Finally

$$s_{\text{crit}} = \ln(0.067\theta^{-2} \alpha_{\text{vir}} \mathcal{M}^2), \quad (4)$$

where $\theta = 0.33$ accounts for shock thickness with respect to cloud size (Federrath & Klessen 2012), and $\alpha_{\text{vir}} \equiv 2E_{\text{kin}}/|E_{\text{grav}}|$ is the virial parameter of a cloud.

The number of star particles created in each cell is drawn from a Poisson distribution with a typical value of $N_* = \dot{\rho}_* \Delta t \Delta x^3 / M_*$ (e.g. Raser & Teyssier 2006). Here Δt is the time step, Δx is the physical size of the gas cell, and $M_* = 500 M_\odot$ is the mass of an individual star particle. Note that below we will consider variations to this fiducial choice for the particle mass.

In this work, we consider a second mode of star formation, i.e. Population III (Pop. III). The transition between these two modes occurs at a metallicity of $10^{-6} Z_\odot$ where it is expected that high-density gas clouds can fragment via dust processes (Omukai et al. 2005). Flagging of star formation sites and the calculation of the star formation efficiency are similar for both star formation modes, but below this metallicity threshold, individual Pop. III stars (rather than an integrated stellar population) are drawn from an IMF following:

$$\frac{dN}{d \log M} \propto M^{-1.3} \exp\left[-\left(\frac{M_{\text{char}}}{M}\right)^{1.6}\right], \quad (5)$$

where $M_{\text{char}} = 100 M_\odot$ as in Wise et al. (2012); Kimm et al. (2017); Katz et al. (2023a). Only a single Pop. III star is allowed to form at each time step.

2.4.2. Jeans Inspired Star Formation

One of the key characteristics of the turbulence-inspired star formation criteria is that gas can reach very high densities $> 10^5 \text{ cm}^{-3}$ as star formation is often held up by the inferred turbulent pressure. This particularly manifests in cosmological simulations where emission line tracers (e.g. [C III] $\lambda\lambda 1908$) probe gas up to 10^5 cm^{-3} (e.g. Katz et al. 2023b) and it is not clear whether such high gas densities are a general characteristic of high-redshift galaxies (Isobe et al. 2023a, although c.f. Senchyna et al. 2024; Topping et al. 2024b,a). Moreover, the terminal momentum from SN explosions scales weakly with gas density (e.g. Thornton et al. 1998) so that if the gas is artificially too high in the simulation, SN are less effective. For this reason, we consider a

model with boosted star formation efficiency in high-density regions: when the Jeans length is unresolved on the highest level of refinement, we artificially increase the efficiency (ϵ_*) defined in Equation 3 by a factor

$$f = \frac{n_{\text{H}}}{100 \text{ cm}^{-3}} + 1, \quad (6)$$

where n_{H} is the gas number density in cm^{-3} . The value of 100 cm^{-3} is chosen as the lower limit of the enhancement as this represents the typical densities of GMCs in the local Universe (e.g. Chevance et al. 2020). It also represents the typical density where the Jeans length (not turbulent Jeans length) is unresolved at the finest refinement level⁸. Recent simulations that adopt a sink particle algorithm for star formation show that the efficiency can be higher than what is inferred from the multi-freefall method (Kang et al. 2024).

2.4.3. Strömgren Turbulence Inspired Star Formation

One of the key issues with radiation transfer simulations is that for typical star formation efficiencies $\lesssim 10\%$, the Strömgren sphere is unresolved (see discussion in e.g. Rosdahl et al. 2015). This means that photoionization, radiation pressure, and photoheating are all unresolved which can have significant numerical impacts (e.g. Deng et al. 2024a). Furthermore, corrections are often made in post-processing to measure emission line luminosities when such a scenario arises (e.g. Smith et al. 2022; Katz et al. 2023b).

To address this, we can require that our star formation algorithm spawns stellar particles as to always locally resolve the Strömgren sphere. The Strömgren radius (Strömgren 1939) is computed as

$$r_{\text{S}} = \left(\frac{3Q}{4\pi n_{\text{H}}^2 \alpha_{\text{B}}}\right)^{1/3}. \quad (7)$$

Here Q is the production rate of hydrogen-ionizing photons (i.e. Lyman-continuum) that directly scales with the stellar particle mass, and α_{B} is the Case B recombination rate of hydrogen at 10^4 K .

In Figure 3, we show the fraction of the gas cell mass that needs to be converted into star particles so that $r_{\text{S}} > \Delta x/2$ for SEDs of varying metallicity from Starburst99 (Leitherer et al. 1999). We note that these curves are only weakly dependent on SED. At a density of 100 cm^{-3} , more than 50% of the gas cell must be converted into star particles for the Strömgren sphere to be resolved. Such efficiencies are rarely reached in our simulations leading to a scenario where r_{S} can be catastrophically under-resolved.

For this reason, we develop a third star formation algorithm that differs from the fiducial model in two ways. First, we include a more extreme boost on the star formation efficiency such that

$$f = \left(\frac{n_{\text{H}}}{100 \text{ cm}^{-3}} + 1\right)^2. \quad (8)$$

In this case, the star formation efficiencies are often $\gg 1$, leading to star formation faster than the free-fall time (see e.g. Kang et al. 2024). Second, we similarly draw from a Poisson distribution the number of star particles to form; however, if the number of particles is fewer than that needed to resolve the Strömgren radius, we do not allow the cell to form a particle. While the motivation for this algorithm is purely numerical, the effect is such that the physics of H II regions is better resolved than in our fiducial model, at the expense of star particles becoming exceptionally massive (i.e. star particles have masses $\gtrsim 10^5 M_\odot$ when formed in dense gas at $n_{\text{H}} > 10^4 \text{ cm}^{-3}$ when the resolution is 10 pc).

⁸ For neutral hydrogen at 100 K, at a density of 100 cm^{-3} , the Jeans length is $\sim 10 \text{ pc}$ which is approximately the physical resolution of our simulation

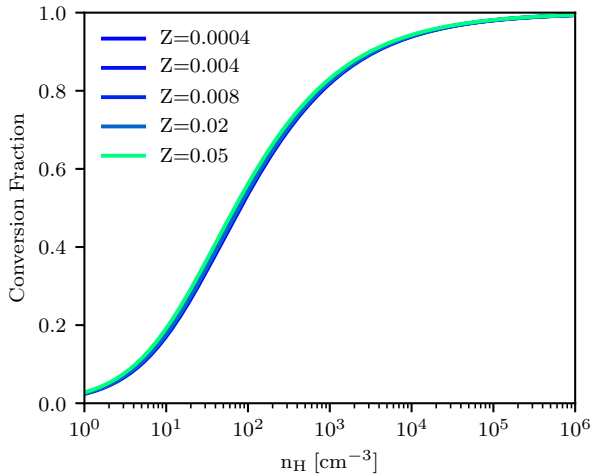


FIG. 3.— Fraction of the gas cell mass that needs to be converted into zero-age main-sequence star particles at different metallicities (different colored lines) such that the Strömgen sphere is resolved. For this figure, we assume a spatial resolution of 5.34 pc, which is the maximum level of refinement at $z = 13.3$ for the fiducial simulations presented below. In the code this will change depending on redshift to correspond to the physical resolution of the cells.

2.4.4. Density Threshold Star Formation

Although the turbulent star formation recipes are calibrated on much higher-resolution simulations where turbulence dictates the efficiency of star formation, in our case, turbulence is measured on the grid scale. Thus, our computed turbulent properties might not reflect the more physical conditions when smaller scales are resolved or more sophisticated schemes that track turbulence on subgrid scales (e.g. [Semenov 2024](#)). For this reason, we consider a more traditional criterion for star formation such that gas with $n_H > \rho_{sf}$, where ρ_{sf} is the density threshold for star formation, and $T < 500$ K are eligible for star formation with no other conditions imposed. We consider two efficiencies of 10% (e.g. [Grisdale et al. 2018](#)) and 100% (e.g. [Hopkins et al. 2014](#)) and two density thresholds of 10^2 cm^{-3} and 10^3 cm^{-3} .

2.5. Radiation Transfer

Multi-frequency radiation transfer (RT) is computed on-the-fly in the simulation in eight energy bins spanning the IR to the EUV, following the methods presented in [Rosdahl et al. \(2013\)](#). Each of the eight photon groups and its purpose are listed in Table 1. Photons are advected using the M1 moment method ([Levermore 1984](#)) and we employ a GLF scheme to construct intercell fluxes. To reduce the computational demands of the RT, we employ a reduced speed of light approximation setting $c_{sim} = 0.01 c$ and subcycle ([Commerçon, Debout & Teyssier 2014](#)) the radiation (and cooling) steps up to 500 times per each hydrodynamic time step. In practice, once SN explosions occur, the number of sub-cycles is typically 1 – 2. In addition to photoionization and photoheating, we consider the dynamical effects of radiation pressure in the single scattering limit for UV and optical photons and multiple scatterings in the IR ([Rosdahl & Teyssier 2015](#)).

For a subset of models, we also consider the impact of Ly α

TABLE 1
EIGHT PHOTON GROUPS USED FOR RADIATIVE TRANSFER IN THIS WORK. LISTED ARE THE PHOTON GROUP NAMES, THEIR LOWER AND UPPER ENERGIES, AND THEIR MAIN PHYSICAL EFFECTS.

Group Name	E_{low} (eV)	E_{high} (eV)	Function
IR	0.1	1.0	Infrared radiation pressure
Optical	1.0	5.6	Direct radiation pressure
FUV	5.6	11.2	Photoelectric heating, Mg I, Si I, S I, Fe I ionization
LW	11.2	13.6	H ₂ & CO dissociation, C I ionization
EUV ₁	13.6	15.2	H I, N I, O I, Mg II ionization
EUV ₂	15.2	24.59	H ₂ , C II, Si II, S II, Fe II, Ne I ionization
EUV ₃	24.59	54.42	He I, O II, C III, N II, N III, Si III, Si IV, S III, S IV, Ne II, Fe III ionization
EUV ₄	54.42	∞	He II, O III+, N IV+, C IV+, Mg III+, S V+, Si V+, Fe IV+, Ne III+ ionization

radiation pressure following [Kimm et al. \(2018\)](#)⁹. Briefly, we calculate the number of recombinations in each cell that are expected based on density, temperature, and ionization fraction as well as the fraction of the recombinations that produce Ly α photons. We then estimate the multiplication factor (M_F) based on the local gas column density and metallicity. The net force on the gas is then $F_{Ly\alpha} = M_F L_{Ly\alpha} / c$, where $L_{Ly\alpha}$ is the Ly α luminosity and c is the speed of light.

There are two sources of radiation in the simulation: star particles and a UV background. Pop. III stars inject radiation based on their mass following [Schaerer \(2002\)](#), while the amount of radiation from Pop. II stars is calculated by interpolating tables computed with STARBURST99 ([Leitherer et al. 1999](#)) as a function of age, metallicity and initial mass function. These luminosities are scaled based on the stellar particle mass. In our fiducial model, we adopt an IMF with an upper-mass cutoff of $120 M_\odot$, an upper-mass slope of -2.3 , a break mass of $0.5 M_\odot$, a lower cutoff mass of $0.08 M_\odot$, and a low mass slope of -1.3 . Note that we do not include a sub-grid escape fraction, i.e. we inject the exact amount of radiation as prescribed by STARBURST99. In future work, we will consider variations on this fiducial IMF.

To account for the radiation of galaxies and quasars from regions outside the Lagrange (zoom-in) volume of our selected halo, we also include a (non-advected) UV background ([Haardt & Madau 2012](#)), considering only LyC (> 13.6 eV) radiation. We exponentially suppress this background field at $z > 5.3$ to model a late cosmic reionization (e.g. [Kulkarni et al. 2019](#)). In this work, all simulations are stopped at $z = 6$ and the UV background thus plays a limited role, but we will pursue simulations to lower redshifts in future work. Furthermore we exponentially suppress the background at $n_H > 100 \text{ cm}^{-3}$ to account for the self-shielding of gas in dense environments ([Rosdahl & Blaizot 2012](#)). Note that we do not follow the ionizing radiation that can be emitted by free-bound recombination and thus assume that it is all absorbed locally (the on-the-spot approximation).

To calculate the photoionization and photoheating rates, the mean energy-weighted and number-weighted cross sections must be known for each species. This depends on the

⁹ Note that this model underestimates the force multiplier by a factor of ~ 3 compared to analytical estimates (e.g. [Lao & Smith 2020](#); [Nebrin et al. 2025](#)), but overestimates the impact of Ly α pressure by a factor of ~ 7 due to employing a point source approximation. In this respect, the approach of [Kimm et al. \(2018\)](#) may be considered as an upper bound (see further discussion below).

SED of each star particle, but is numerically costly to perform this calculation locally for each individual cell. Instead, we compute the mean SED to estimate the cross sections. At very high redshifts where star formation is dominated locally by individual Pop. III events, we recompute cross sections at every coarse time step as a luminosity-weighted mean over all star particles since stellar evolution proceeds rapidly for massive stars. At lower-redshift, we perform this calculation every ten coarse time steps¹⁰. Finally, to ensure that the radiation phase is well sampled in the simulation we ensure that once star particles form, fine time steps are a maximum of 10^5 yr. In practice, once SNe explode, the fine time steps on the maximum level of refinement are of $\mathcal{O}(100)$ yr.

2.6. Stellar Feedback & Chemical Enrichment

2.6.1. Pop. III

We assume that Pop. III stars can end their lives via four channels based on the mass of the star particle: core-collapse SN, hypernova, direct collapse to a black hole, or as a Pair Instability SN (PISN). In cases where Pop. III stars explode, yields are adopted from Umeda & Nomoto (2002); Nomoto et al. (2006); Nomoto, Kobayashi & Tomimaga (2013). Pop. III stars between $10 - 20 M_{\odot}$ explode as core-collapse SN injecting the equivalent of 10^{51} erg. In the mass range $20 - 40 M_{\odot}$, Pop. III stars explode as hypernova with injection energies of $10 - 40 \times 10^{51}$ erg based on mass following Nomoto et al. (2006). We assume that Pop. III stars in the mass range $40 - 140 M_{\odot}$ directly collapse to black holes injecting no metals or energy. Finally, Pop. III stars in the mass range $140 - 300 M_{\odot}$ explode as PISN with energy based on the remnant He core following Heger & Woosley (2002). Whenever a SN explodes, we ensure that the expected final terminal momentum of the explosion is captured, independent of resolution (see below). Pop. III main sequence lifetimes are adopted from (Schaerer 2002).

2.6.2. Pop. II

We base the injection of momentum, energy, and metals from Pop. II stellar populations on the VINTERGATAN model (described in detail in Agertz et al. 2021 and Rey et al. 2023; see also Agertz et al. 2013; Agertz & Kravtsov 2015; Agertz et al. 2020). The model includes core-collapse SN, type Ia SN, and stellar winds. This model leads to realistic star formation modes across cosmic times (Renaud, Segovia Otero & Agertz 2022; Segovia Otero, Renaud & Agertz 2022) and is validated against $z = 0$ observables, producing stellar masses compatible with abundance matching expectations for Milky-Way mass dark matter halos (e.g. Rey et al. 2023) and discs whose structure resembles our Milky-Way's thin and thick disk (Agerzt et al. 2021; Renaud et al. 2021b,a).

For each stellar population of a given age, we stochastically sample individual SNeII progenitors exiting the main sequence during each time step, following the main-sequence lifetime-mass relation from Schaerer et al. (1993). We assume that stars with $8 \leq m_{*}/M_{\odot} \leq 25$ explode as SNeII with an energy of $E_{\text{SN}} = 10^{51}$ erg, consistent with the adopted yields model (described below). For a subset of models, we allow Pop. II stars with mass $\geq 25 M_{\odot}$ to explode as hypernova (HN) following the model of Nomoto et al. (2006) where the injected energy, metal yields, and fraction of stars that explode as HN evolve with stellar mass and metallicity.

¹⁰ In practice, we wait for the Pop. III star formation to become subdominant compared to Pop. II and update this parameter when restarting the simulation from a checkpoint.

2.6.3. Energy and Momentum Injection from Supernova

We always inject momentum from the initial ballistic ejecta scaled as $\sqrt{2 E_{\text{SN}}/M_{\text{ej}}}$, where M_{ej} is the mass loss associated with a progenitor of m_{*} according to Limongi & Chieffi (2018). When the supernova cooling radius, computed as

$$r_{\text{cool}} = 30 \left(\frac{n}{1 \text{ cm}^{-3}} \right)^{-0.42} \times (\text{Max}(Z_{\text{gas}}, 0.01 Z_{\odot}))^{-0.18} \left(\frac{E}{E_{\text{SN}}} \right)^{0.2857} \text{ pc}, \quad (9)$$

is resolved by at least four grid cells, we additionally inject 10^{51} erg of thermal energy as the Sedov-Taylor phase should be resolved. If the cooling radius is unresolved, we inject the terminal momentum according to

$$p = 2.95 \left(\frac{E}{E_{\text{SN}}} \right)^{0.941} \left(\frac{n}{1 \text{ cm}^{-3}} \right)^{-0.1176} \times (\text{Max}(Z_{\text{gas}}, 0.01 Z_{\odot}))^{-0.2} M_{\odot} \text{ km s}^{-1}, \quad (10)$$

(see e.g. Blondin et al. 1998 and Kim & Ostriker 2015). All injections of mass, momentum, and metals (see below) are performed in the local 8 grid cells surrounding the stellar particle. For numerical reasons, we apply a limiter such that supernova ejecta cannot exceed 4000 km s^{-1} and the gas cannot be heated above 10^9 K .

In Figure 4, we show the terminal momentum recovered in an example simulation where we launch a SN in a homogeneous box of varying density. At the lowest densities, where the cooling radius is well resolved, we recover the expected value. As the density increases, we begin to under predict the momentum due to the worsening resolution. For this particular setup, the transition between energy and momentum injection occurs at $n_{\text{H}} \sim 125 \text{ cm}^{-3}$ at which point we slightly overshoot the terminal momentum due to the sharp transition. We then begin to converge back to the expectation value as density increases. The mean absolute deviation from the expectation value is 40% and adopting a smoother transition (e.g. Kimm & Cen 2014) would marginally improve this behavior (see also Hopkins et al. 2018).

2.6.4. Metal Yields

Each SNeII further injects individual elements according to the progenitor-mass and metallicity dependent grid of Limongi & Chieffi (2018). We modify the yields to account for the radioactive decay of specific isotopes on timescales much shorter than galactic evolution, namely (i) the decay half-life, $t_{1/2}$ of ^{22}Na into ^{22}Ne is 2.6 yr and its contribution is thus added to Ne yield; (ii) the contribution of ^{26}Al is added to Mg ($t_{1/2} = 0.73 \text{ Myr}$); and (iii) the contributions of ^{56}Ni and ^{56}Co are added to the Fe yield ($t_{1/2} \leq 100 \text{ days}$). Stars with $m_{*} \geq 25 M_{\odot}$ are assumed to directly collapse without exploding, but still inject metals into the ISM following their mass-loss due to winds (Limongi & Chieffi 2018).

The yields from Limongi & Chieffi (2018) already include the metal production from pre-supernova O and B stellar winds. Compared with Agertz et al. 2013; Agertz & Kravtsov 2015, we do not account for the momentum injection of these winds which are expected to be a subdominant feedback channel given the low-metallicities considered here. We however account for the mass, momentum and metal injection from asymptotic giant branch (AGB) stars, computing their IMF-averaged mass and momentum contributions as in Agertz et al. (2013) and using yields from Ritter et al. (2018).

We also account for SNeIa at a rate of $2.6 \times 10^{-13} \text{ SNIa yr}^{-1} M_{\odot}^{-1}$, assuming the delay-time distribution

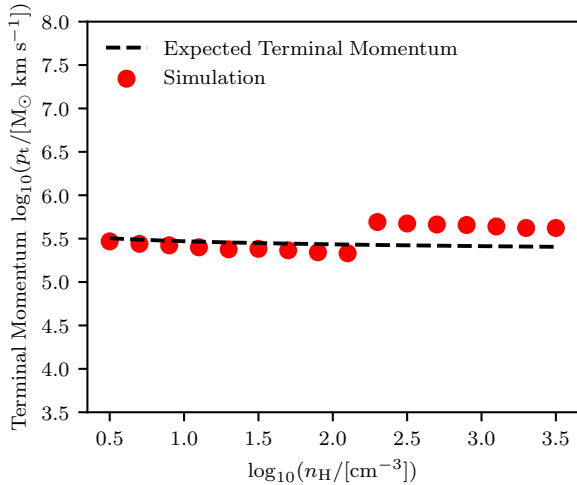


FIG. 4.— Expected terminal momentum from SN explosions (dashed black line) as a function of gas density compared to that measured in idealized MEGATRON simulations (red circles). The discontinuity at $n_{\text{H}} = 10^{2.3} \text{ cm}^{-3}$ represents the transition point between a resolved and unresolved cooling radius for the SN remnant. The expected terminal momentum follows the results of Kim & Ostriker (2015).

of Maoz & Graur (2017), injecting metals (and thermal energy or momentum depending on resolution) according to Seitzzahl et al. (2013).

3. REGULATING STAR FORMATION

To explore how the MEGATRON model regulates high-redshift galaxy formation, we perform cosmological zoomed simulations of a high-redshift dwarf galaxy ($M_{\star} \approx 10^7 M_{\odot}$ at $z = 6$). In this section, we present results from our fiducial implementation (as defined in Table 2), before performing a wide exploration of numerical parameters and physics modules in Section 4.

The initial conditions for our target dwarf galaxy represent a halo that grows to a virial mass of $\sim 10^9 M_{\odot}$ at $z = 6$. The halo was selected from a parent volume of 5^3 Mpc^3 that was run with 128^3 dark matter particles. Higher resolution initial conditions were generated with two additional levels of refinement within the Lagrangian region of the halo such that the halo remains uncontaminated by low-resolution dark matter particles well beyond its virial radius by $z = 6$. The highest resolution dark matter particles have a mass of $2.1 \times 10^4 M_{\odot} h^{-1}$ and we assume a flat cosmology consistent with Planck Collaboration et al. (2020) such that $H_0 = 67.66 \text{ km s}^{-1} \text{ Mpc}^{-1}$, $\Omega_{\text{m}} = 0.3111$, $\Omega_{\text{b}} = 0.04897$. We allow for seven additional levels of refinement beyond what is present in the initial conditions such that we reach a spatial resolution of ~ 11 physical pc at $z = 6$.

In Figure 5, we plot the cumulative stellar mass growth within the full Lagrangian region as a function of the age of the universe and redshift down to $z = 6$. Metal-free star formation begins at $z = 16.4$ with the formation of a $111 M_{\odot}$ Pop. III star. Due to its mass, this star collapses directly into a black hole. Subsequent Pop. III stars form and by $z = 15.4$, the first Pop. III SN explodes, polluting the gas with the first heavy elements. By $z = 13.4$, the halo recovers from the SN explosion and the first metal-enriched Pop. II stellar cluster forms. Pop. III star formation continues until $z \sim 7.7$ but remains well sub-dominant compared to Pop. II star formation at $z < 10$.

The star formation history of the halo is very “bursty”. Large fluctuations of nearly two orders of magnitude in SFR

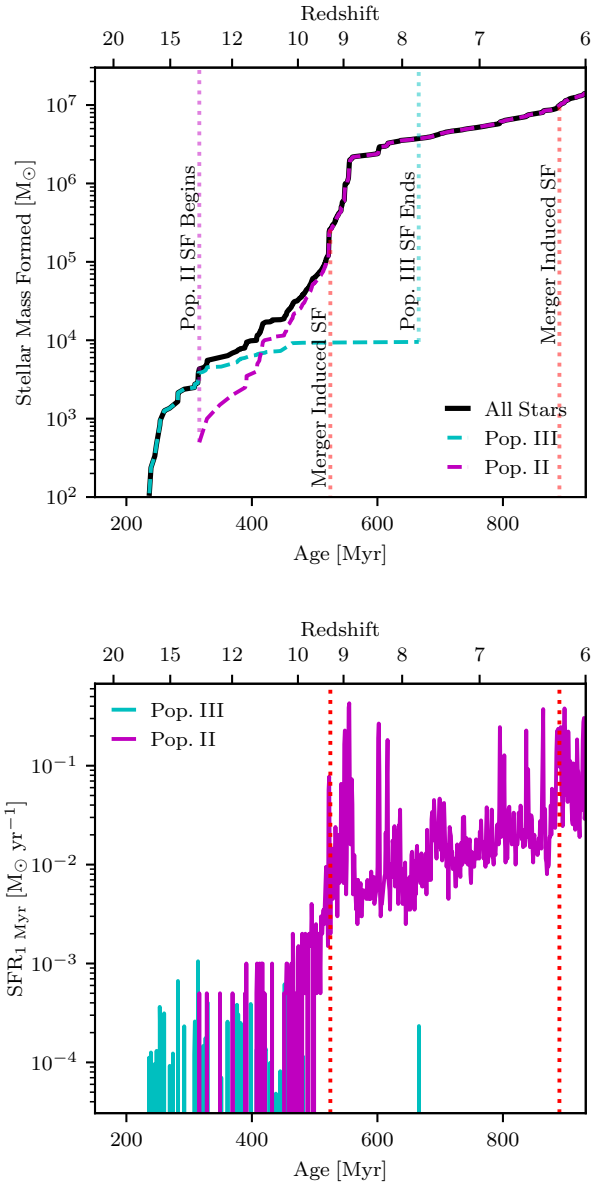


FIG. 5.— Cumulative stellar mass formed (top) or 1 Myr-averaged star formation rate (bottom) as a function of time for all stars in the simulation. Pop. III star formation (cyan) begins first and continues until $z \approx 8$, but is rapidly overtaken by Pop. II star formation (purple). Rapid increases in stellar mass (vertical red dashed) track vigorous assembly through major mergers.

occur on Myr timescales (see bottom panel of Figure 5). The first burst occurs with the formation of the first Pop. III stars and the SFR slows down after the first Pop. III SN event. Another strong burst of star formation occurs at $z \sim 9.3$ which is induced by a major merger. Similar behavior is seen at $z \sim 6.2$ where two smaller haloes initiate a three-way merger, which again induces star formation.

To understand how well the feedback is regulating star formation, we use the ROCKSTAR halo finder (Behroozi, Wechsler & Wu 2013) to identify haloes in the simulation. We then assign star particles to haloes by selecting all star particles within the halo virial radius. For stars particles that are within the virial radius of more than one halo (which can happen during mergers or when there are subhaloes), we assign them to the halo that minimizes d/r_{vir} , where d is the

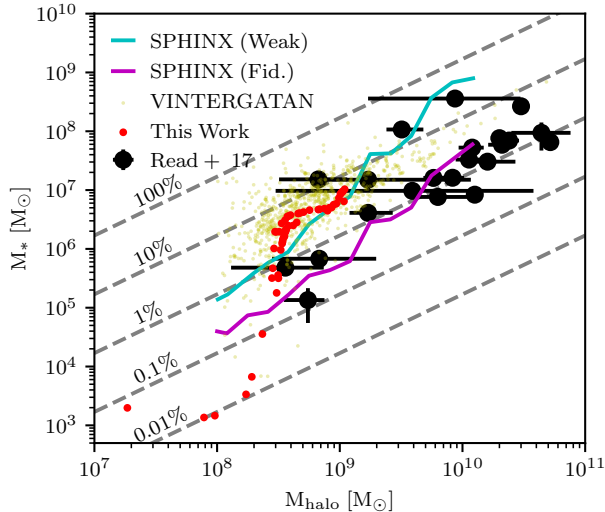


FIG. 6.— Stellar mass-halo mass relation for the main halo between $z \sim 15 - 6$ (red points). Dashed black lines show contours of constant efficiency defined as $M_*/(\frac{\Omega_b}{\Omega_{DM}} M_{\text{halo}})$. Throughout the simulation, our main halo aligns with the weak feedback model from the SPHINX simulation (cyan) rather than their fiducial relation (purple) which was necessary to reproduce the $z = 6$ UV luminosity function. Nonetheless, the simulation is higher but broadly aligned with $z = 0$ dwarf galaxies (black points; Read et al. 2017) and $z = 6$ data from the VINTERGATAN-GM simulations (Rey et al. 2023) on which our feedback model is based. This highlights that successful low-redshift galaxy formation models (e.g. VINTERGATAN) do not guarantee well-regulated high-redshift galaxies, warranting an in-depth exploration of numerical parameters in this regime (Figure 7).

distance to the center of each halo.

In Figure 6, we plot the stellar mass-halo mass relation for the main halo for all snapshots after first star formation. We compare them to the inferred properties of $z = 0$ dwarf galaxies from Read et al. (2017), simulated galaxies at $z = 6$ from the SPHINX simulation that was designed to study the high-redshift Universe, and simulated galaxies at $z = 6.1$ in the Lagrangian patches of the VINTERGATAN project that agrees well with data from the low-redshift Universe (Rey et al. 2023, Rey et al. in prep.).

With the fiducial model, our dwarf galaxy at $z = 6$ broadly consistent with but perhaps slightly higher than the average stellar mass at a given halo mass of local dwarf galaxies at $z = 0$. This is to be expected due to the mismatch in timescales and physical mechanisms that govern star formation in the two redshift regimes – dwarf galaxies with stellar masses of $\approx 10^6 M_\odot$ at $z = 0$ are likely to have been strongly affected by reionization quenching over their history (e.g. Efstathiou 1992; Benitez-Llambay & Frenk 2020; Rey et al. 2020; Katz et al. 2020, and references therein). This would lead to a sharp decline (or altogether flattening) in their stellar mass growth rate for a given halo mass unit, compared to our high-redshift dwarf for which reionization quenching has yet to take effect.

Nevertheless, the elevated stellar mass is worrying, particularly since it follows the ‘Weak feedback’ model from the SPHINX simulations. The ‘Weak feedback’ model from the SPHINX simulation over-predicts the UV luminosity function of high-redshift galaxies (Rosdahl et al. 2018). In contrast, our test dwarf galaxy is compatible with the VINTERGATAN data at $z = 6.1$. The numerics of the feedback implementation for SNII, SNIa, and winds are nearly identical between

VINTERGATAN and this work, but we stress that this agreement is non-trivial due to the vastly different heating and cooling physics (equilibrium vs. non-equilibrium + radiative transfer) and numerical resolutions.

From these comparisons, we conclude that:

1. Our fiducial model may require additional feedback energy and/or channels to regulate high-redshift star formation, as is successfully done in e.g. the SPHINX ‘Fiducial’ model. Alternatively, a model where a higher fraction of the stellar particle mass evolves off the main sequence so that the mass-to-light ratio decreases at later times (e.g. a top-heavy IMF) would achieve a similar ‘apparent’ regulation.
2. Successful low-redshift models such as VINTERGATAN do not guarantee a well-regulated star formation at $z > 6$, and that such lack of regulation at high redshift does not imply over-massive galaxies at low redshift.

As stellar masses are difficult to infer at high-redshift (e.g. Narayanan et al. 2024), it remains unclear what the true stellar mass-halo mass relation is at high-redshift.

Direct constraints on the ISM conditions of high-redshift galaxies from JWST are one potential route to reconcile these high- and low-redshift successes together. The remainder of this paper thus focuses on how variations in subgrid modeling affects the regulation of star formation (Section 4), combined with an in-depth discussion of their associated spectroscopic observables at $z > 6$ (Section 5).

4. SYSTEMATIC VARIATIONS OF SUBGRID PARAMETERS

In this Section, we vary several parameters of our fiducial model to understand how the stellar mass growth and star formation regulation responds to assumptions for our subgrid model. In total, we run 25 simulations and refer to Table 2 for a comprehensive list of the parameters varied in our simulation suite.

4.1. Star Particle Mass

Numerous simulations show that the clustering of SNe is key to drive strong galactic outflows, as coherent and repeated explosions create super-bubbles that break out from the disk and strongly enhance outflow loading factors (e.g. Keller et al. 2014; Yadav et al. 2017; Fielding et al. 2017; Gentry et al. 2019; Gentry, Madau & Krumholz 2020; Smith et al. 2021; Keller & Kruijssen 2022). Increasing the stellar particle mass will lead to a larger cluster of SNe exploding at a similar location and time, rather than being spatially and temporally distributed in smaller-mass clusters.

In the top left panel of Figure 7, we show the ratio of stellar mass formed in simulations with star particle masses that are $2\times$, $8\times$, and $20\times$ that of the fiducial model. At $t = 929$ Myr, corresponding to $z = 6$, we see very little difference in the total stellar mass in any of the models. Increasing the star particle mass by factors of 2 or 8 provides no additional regulation. Increasing by a factor of 20 results in $\sim 40\%$ lower stellar mass. Such a stellar mass is perhaps numerically ill-advised because it is $> \frac{\Omega_b}{\Omega_{\text{dm}}} m_{\text{dm}}$, where m_{dm} is the dark matter particle mass.

There does seem to be a systematic effect where prior to the major merger, the simulations with higher star particle mass overshoot the fiducial model in terms of stellar mass and then subsequently undershoot. The origin of this behaviour is unclear. The stellar mass of the fiducial simulation increases by $> 100\times$ in the 150 Myr time-frame around the merger, so these variations are likely due to random fluctuations in star formation history.

TABLE 2

LIST OF PARAMETERS USED FOR OUR 25 SIMULATIONS. M_* IS THE STELLAR MASS RESOLUTION, ϵ_{ff} IS THE STAR FORMATION EFFICIENCY PER FREE-FALL TIME, t_{SN} IS THE TIME TO THE FIRST SUPERNOVA, E_{SN} IS THE ENERGY PER SNEII, HN REFERS TO HYPERNOVAE BEING TURNED ON OR NOT, $\text{Ly}\alpha$ REFERS TO LYMAN- α RADIATION PRESSURE BEING TURNED ON OR NOT, M_{DM} IS THE DM MASS RESOLUTION, l_{max} IS THE MAXIMUM LEVEL OF REFINEMENT, $c_{\text{sim.}}$ IS THE VALUE OF THE SPEED OF LIGHT IN THE SIMULATION. SEE THE TEXT FOR FURTHER DETAILS.

Name	M_* (M_{\odot})	ϵ_{ff}	t_{SN} (Myr)	E_{SN} (10^{51} erg)	HN	$\text{Ly}\alpha$ RP	SF model	$\rho_{\text{SFR,min}}$ (cm^{-3})	M_{DM} ($10^4 M_{\odot}$)	l_{max}	$c_{\text{sim.}}$ (c)	Cooling model
Fiducial	500	Eq. (3)	7	1			turb.	10	2.1	15	0.01	PRISM
$M_* \times 2$	1000	Eq. (3)	7	1			turb.	10	2.1	15	0.01	PRISM
$M_* \times 8$	4000	Eq. (3)	7	1			turb.	10	2.1	15	0.01	PRISM
$M_* \times 20$	10000	Eq. (3)	7	1			turb.	10	2.1	15	0.01	PRISM
Efficient	500	100 %	7	1			turb.	10	2.1	15	0.01	PRISM
Efficient, massive	1000	100 %	7	1			turb.	10	2.1	15	0.01	PRISM
Efficient, more massive	4000	100 %	7	1			turb.	10	2.1	15	0.01	PRISM
$t_{\text{SN},0.5}$	500	Eq. (3)	0.5	1			turb.	10	2.1	15	0.01	PRISM
$t_{\text{SN},1.0}$	500	Eq. (3)	1.0	1			turb.	10	2.1	15	0.01	PRISM
$t_{\text{SN},2.0}$	500	Eq. (3)	2.0	1			turb.	10	2.1	15	0.01	PRISM
$E_{\text{SN}} \times 2$	500	Eq. (3)	7	2			turb.	10	2.1	15	0.01	PRISM
$E_{\text{SN}} \times 4$	500	Eq. (3)	7	4			turb.	10	2.1	15	0.01	PRISM
$E_{\text{SN}} \times 5$	500	Eq. (3)	7	5			turb.	10	2.1	15	0.01	PRISM
HN	500	Eq. (3)	7	1 – 40	✓		turb.	10	2.1	15	0.01	PRISM
$\text{Ly}\alpha$	500	Eq. (3)	7	1		✓	turb.	10	2.1	15	0.01	PRISM
Density	500	10%	7	1			dens.	10^2	2.1	15	0.01	PRISM
Jeans	500	Eqs. (3, 6)	7	1			Jeans	10	2.1	15	0.01	PRISM
Strömgen	500	Eqs. (3, 8)	7	1			Ström.	10	2.1	15	0.01	PRISM
Efficient	500	100 %	7	1			dens.	10^2	2.1	15	0.01	PRISM
Efficient, denser	500	100 %	7	1			dens.	10^3	2.1	15	0.01	PRISM
Efficient, denser, energetic	500	100 %	7	5			dens.	10^3	2.1	15	0.01	PRISM
Low-resolution	500	Eq. (3)	7	1			turb.	10	16	14	0.01	PRISM
High-resolution	500	Eq. (3)	7	1			turb.	10	0.26	16	0.01	PRISM
Fast-light	500	Eq. (3)	7	1			turb.	10	2.1	15	0.1	PRISM
Simple cooling	500	Eq. (3)	7	1			turb.	10	2.1	15	0.01	Simple

4.2. Star Formation Efficiency

The typical star formation efficiencies per free-fall time measured by our fiducial star formation algorithm maximize at $\sim 30\%$. Increasing the efficiency can lead to star formation at lower densities and more clustered star formation. Hopkins et al. (2018) argues that this parameter has negligible effect on galaxy properties because star formation is feedback-regulated and gas will pile up until the same star formation is achieved, although the FIRE simulations adopt a fiducial value of 100%. In the top middle panel of Figure 7, we show the ratio of stellar mass formed as a function of time for models where we ignore Equation 3 and set the efficiency per free-fall time to 100%. Similar to what was found in Hopkins et al. (2018), we find that the efficiency plays almost no role in changing the final stellar mass of the object at $z = 6$. As discussed in the previous section, it is unclear what causes the runs with higher stellar mass to grow their stellar mass earlier compared to the fiducial model and this may be due to the stochasticity in the star formation history when the stellar mass is very low.

We further test whether combining an enhanced efficiency with a higher star particle mass ($2\times$ and $8\times$) can help regulate the galaxy. While the $2\times$ higher star particle mass results in no change in the final stellar mass, combining the high efficiency with an $8\times$ more massive star particle results in similar stellar mass suppression as increasing the star particle mass by a factor of 20. Nevertheless, this result is relatively modest given the extreme change in efficiency.

Although the integrated stellar mass does not change significantly, the higher efficiency should in principle lead to burstier star formation. This is interesting in the context of high redshift as UV variations driven by bursty star formation has been used as an explanation for the abundance of UV bright galaxies in the early Universe (e.g. Shen et al. 2023; Sun et al. 2023). It should be noted that simulations do not agree upon how much M_{UV} fluctuates as a function of

mass but a generic prediction is that as mass increases, UV magnitude fluctuations decrease (e.g. Kravtsov & Belokurov 2024; Gelli, Mason & Hayward 2024; Shen et al. 2025). In Figure 8, we show the intrinsic 1500 Å UV luminosity of the Lagrangian region as a function of time. The merger at $z \sim 9$ leads to a star formation event which brings all simulations to a magnitude $\lesssim -16$. Even after a merger, where UV luminosity is expected to peak due to merger-induced star formation, increasing the star formation efficiency to 100% and increasing the stellar mass by a factor of 8 only leads to a modest increase of 0.4 magnitudes. This increase is well below the natural, intrinsic variability of $M_{\text{UV},1500}$. Hence changing the star formation efficiency in the context of our model is highly unlikely to lead to fundamental differences in the UV luminosity function.

In summary, increasing the efficiency of star formation per freefall time and the stellar particle mass can have a minor impact on the final stellar mass of the object, although as we show below, these effects are well subdominant compared to other subgrid model parameters.

4.3. SN Timescale

One of the key differences in our work compared to many other cosmological simulations is that only stars with mass $< 25 M_{\odot}$ explode as SN. While the typical $100 M_{\odot}$ evolves off the main sequence in ~ 3 Myr, a $25 M_{\odot}$ star takes significantly longer (~ 7 Myr). This timescale has numerous implications for galaxy formation. Dekel et al. (2023) recently argued that when the free-fall time of the gas is significantly shorter than the feedback timescale¹¹, star formation proceeds in a “feedback-free” mode, which can result in up to 100% of the gas converting into stars. If confirmed, such

¹¹ Note that in our case, this timescale would correspond to the SN timescale because stellar winds, radiation pressure and photo-heating seem to have a limited impact at our resolution.

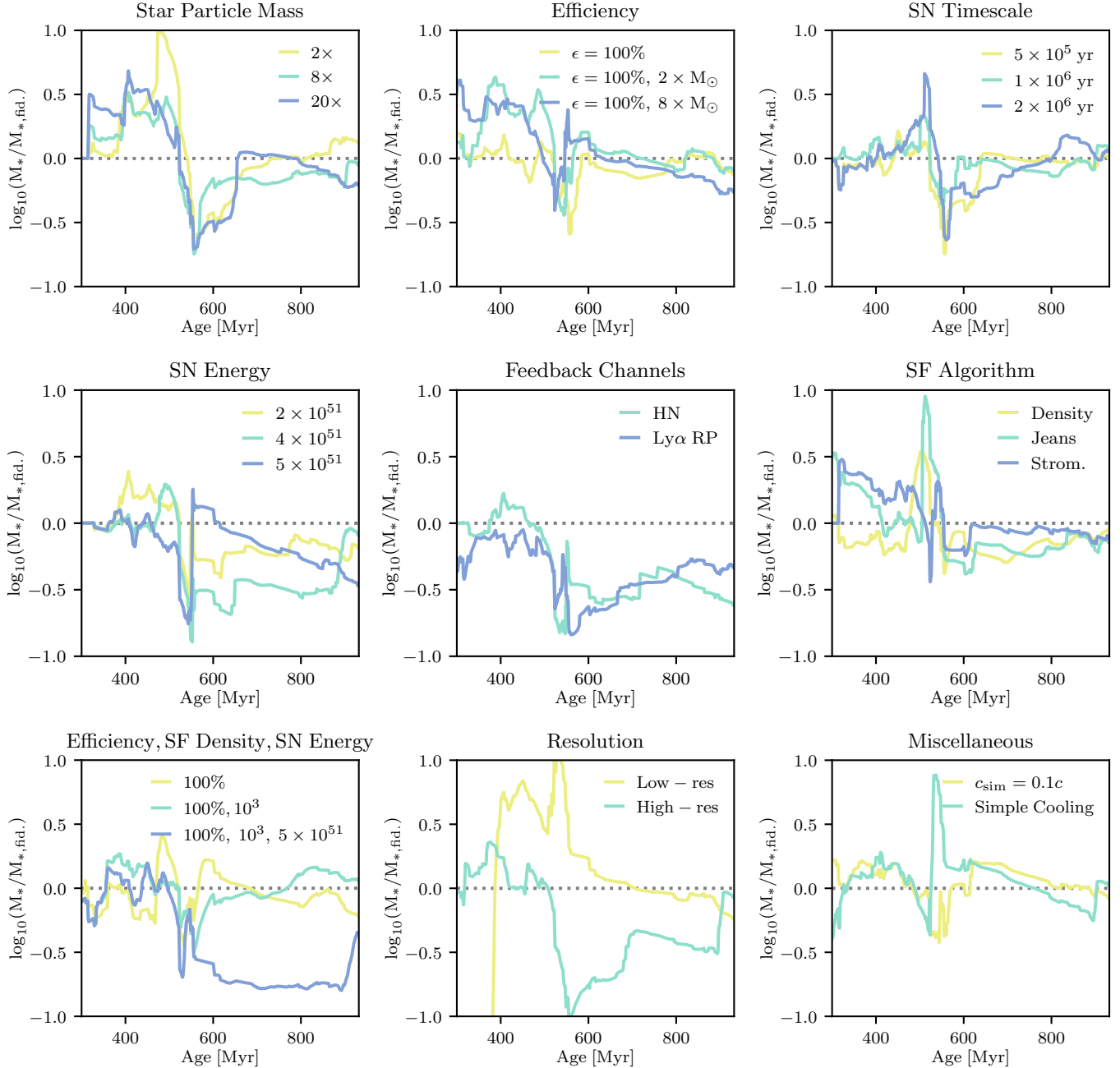


FIG. 7.— Ratio of cumulative stellar mass formed compared to our fiducial model for all numerical parameters explored in this paper. Panels show broad families of variations, with details of each model variation described in the text.

a model would provide a natural explanation for the abundance of bright galaxies observed at high-redshift without the need to invoke bursty star formation or a changing mass-to-light ratio. Due to the evolution of the ISM towards lower densities at lower redshift, this process is predicted to only operate in the early Universe. However, if the timescale to SN is much longer, the “feedback-free” process may continue to operate at progressively lower redshifts which could make the model inconsistent with observations. In the lower redshift Universe, the observed spatial de-correlation between H α and CO emission in disk galaxies is highly suggestive that star-forming clouds are rapidly dispersed (Krujissen et al. 2019). Reproducing this behavior with simulations seems to require strong early feedback (Semenov, Kravtsov & Gnedin 2021; Jeffreson, Semenov & Krumholz 2024) as matching the

timescales with physically-based subgrid models is non-trivial (e.g. Keller, Krujissen & Chevance 2022; Hu et al. 2024). Recent observations also support this picture (Chevance et al. 2022). Given the implications for feedback timescale in both the high- and low-redshift Universe, in this Section, we artificially modulate the time at which the first SN explode to understand its effect on early galaxy formation.

For each star particle in the fiducial model, the first SN are eligible to explode at an age of ~ 7 Myr. In practice, the age of the particle is often older than this value because we stochastically sample the IMF. To modify this behavior, we change the main-sequence lifetime-mass relation such that an $8 M_{\odot}$ star still explodes at the same time as in the fiducial model (34 Myr), but the $25 M_{\odot}$ main-sequence lifetime is reduced to either 5×10^5 yr, 1×10^6 yr, or 2×10^6 yr, respec-

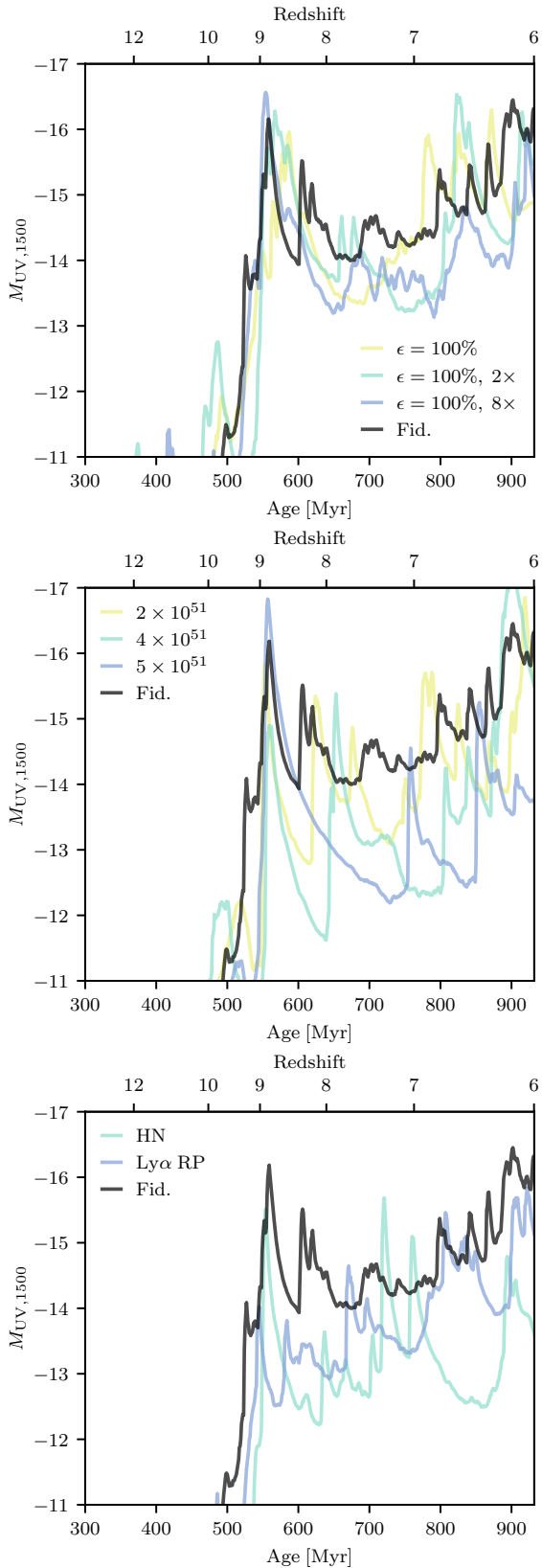


FIG. 8.— Intrinsic UV magnitude as a function of time for all stars in each simulation. In the top panel, we increase ϵ_{ff} to 100% (yellow) or simultaneously increase ϵ_{ff} and mass of the star particle by factors of 2 (green) or 8 (blue). Even with extremely efficient and clustered star formation, the halo gets at most 0.4 mag brighter than our fiducial model (black). These parameters are thus unlikely to lead to large changes in the population-averaged UV luminosity function. The middle and bottom panels show the results for changing the strength of SN or adding in additional feedback channels.

tively. In this way we have elongated the period over which the SN explode, i.e. potentially slightly reducing the spatial and temporal clustering of the SN, which seems to have little impact on our results, but the star-forming clouds are subject to feedback much earlier on in their evolution.

The top right panel of Figure 7 shows the cumulative stellar mass formed of each of these three model variations, normalized to the fiducial model as a function of time. Despite the significant reduction in timescale to first SN, the integrated stellar masses do not change by $z = 6$. Thus, if the total feedback budget remains unchanged, the time at which SN begin does not seem to impact how well the galaxy is regulated.

We emphasize two key points. First, even if the star formation is not better regulated, this does not necessarily mean that the properties of the ISM are unaffected. For example, Keller, Kruijssen & Chevance (2022) show how the properties of an isolated disk can change significantly using an empirical model for feedback injection where timescale is a key parameter. Second, even though the first SN explode earlier in these simulations, the time period over which the SN explode is effectively elongated. While stochastic sampling of the IMF is perhaps the most realistic, differences may be found if we explode all SN for the star particle at the exact same time (e.g. Bhagwat et al. 2024). The results in this section do not conflict with the conclusions of these other studies.

4.4. SN Energy

In order to better regulate early galaxy formation, Rosdahl et al. (2018) adopted the strategy of increasing the total number of SN by a factor of four. One could alternatively increase the total energy of a SN from the fiducial value of 10^{51} erg to an arbitrarily higher value as is common technique in AMR simulations (e.g. Agertz, Teyssier & Moore 2011; Semenov, Kravtsov & Gnedin 2021). The final terminal momentum of a SN scales nearly linearly with SN energy and hence may lead to a significant reduction in star formation (compare the magenta and cyan lines in Figure 6 for results from SPHINX).

Explanations for this modification can be both physical or numerical in origin. Stellar evolution models predict that not all SN explode with energies of 10^{51} erg (e.g. Sukhbold et al. 2016), with excursions to both lower and higher values. In the extreme scenario, some stars may explode as hypernovae (HN), which can have energies of $40\times$ the typically assumed value (Nomoto et al. 2006). This is further discussed in Section 4.5. Adopting a more top-heavy IMF can also lead to an increased number of SN, although the exact increase is highly dependent on the upper mass slope of the IMF. Making the IMF too top-heavy can also decrease the total number of SN for a stellar population as the mean mass of stars simultaneously increases as the high-mass slope flattens (Prgomet et al. 2022). This scenario is however intriguing for multiple reasons. First, modifying the IMF to be more top-heavy can both increase and decrease the SN energy budget which can impact the amount of regulation. Second the mass-to-light ratios are reduced at early times when massive stars are on the main-sequence and then increased at later times with respect to a standard Kroupa IMF, which could simultaneously help reconcile the abundance of early bright galaxies with the slow evolution in stellar mass growth towards lower redshifts (Katz et al. *in prep.*).

From a numerical perspective, although our SN scheme is designed to capture the final terminal momentum of a SN independent of resolution, energy can be artificially dissipated for other reasons. For example, the finite resolution means that shocks are much thicker in the simulation than in an idealized case. This has the effect of mixing the hot interior gas of the SN bubble with the denser gas outside the shell which can enhance cooling (e.g. Gentry et al. 2017, 2019). This is particularly bad in the context of non-equilibrium cooling as

mixing ionized and neutral gas can lead to a strong enhancement in collisional excitation cooling compared to the case of collisional ionization equilibrium. This problem may be further exacerbated as the AMR grid tends to de-refine in SN-affected regions. The de-refinement is a diffusive process which again leads to mixing. For SN that drive strong outflows, the movement of the gas across the grid is also diffusive which could further lead to energy losses. Hence for the multitude of numerical reasons, energy may be artificially radiated even after the “correct” amount of momentum is injected into the ISM and represent variation of the classic “over-cooling” problem (Katz 1992). Increasing the total energy of each SN explosion may help to combat these effects.

Finally, there remains some debate on the exact value of the final terminal momentum of a SN explosion and how it scales with SN energy, metallicity, and gas density. Certain models (e.g. Gentry et al. 2017) show increases of more than a factor of three in certain regimes compared to the fiducial model of Kim & Ostriker (2015) used in this work. The model we adopt has been calibrated for individual SN; however, in the case where multiple SN explosions occur near each other, there are also disagreements on whether the momentum is boosted with respect to the single SN limit for realistic environments (e.g. Gentry et al. 2019; Kim, Ostriker & Raileanu 2017).

With this discussion in mind, we run three simulations, testing how galaxy evolution changes when the energy per SN is increased to 2×10^{51} erg, 4×10^{51} erg, and 5×10^{51} erg, respectively. The cumulative stellar mass growth normalized by the fiducial model is shown in the left panel of the second row of Figure 7. In all cases, the stellar mass at $z = 6$ is lower than in the fiducial model with the $5 \times$ boost model predictably producing the lowest integrated stellar mass of a factor of ~ 2 lower than the fiducial model. However, the change in feedback energy seems to lead to non-trivial results. For example, just after the high-redshift merger, the model with the highest feedback energy temporarily exhibits the highest stellar mass (between 550–600 Myr). This model suppresses star formation immediately preceding this event. We speculate that the gas has built up and the strong dynamical instabilities triggered by the merger lead to catastrophic star formation which cannot be regulated, even with $5 \times$ boosted SN energy. A similar scenario seems to happen in the model with a $4 \times$ boost in the SN energy. Comparing this model with the $2 \times$ boost, they seem to track each other’s star formation history with the $4 \times$ model having two times less stellar mass for most of the recent history of the galaxy. However, towards the second merger at $z \sim 6.3$, it is likely that the excess gas reservoir leads to a stronger star formation event such that by $z = 6$, the total stellar mass formed in the $4 \times$ model is actually more than the $2 \times$ model. We expect that if this simulation is run for longer, the model with higher SN energy will again fall below that of the fiducial and the $2 \times$ boost model. Similar behavior was also observed in the simulation of Agertz, Teyssier & Moore (2011) where the early suppression of star formation from stronger feedback was later compensated at lower redshift by a higher SFR due to the increased gas reservoir. More generally, the SFR decrease is expected to scale sub-linearly with boosts to feedback energy (e.g. Benincasa et al. 2016).

While the gas reservoir argument is difficult to prove in practice, we can gain insight by looking at the evolution of the gas mass inside haloes as a function of redshift. In Figure 9, we plot the total gas (solid lines) and the cold gas (dashed lines, defined as having a temperature < 500 K) mass within haloes as a function of redshift. When the feedback energy is increased by a factor of 2–4, the total gas reservoir within the haloes is almost the same as in the fiducial model while we find a slight decrease for a SN energy of $5 \times$ the fiducial

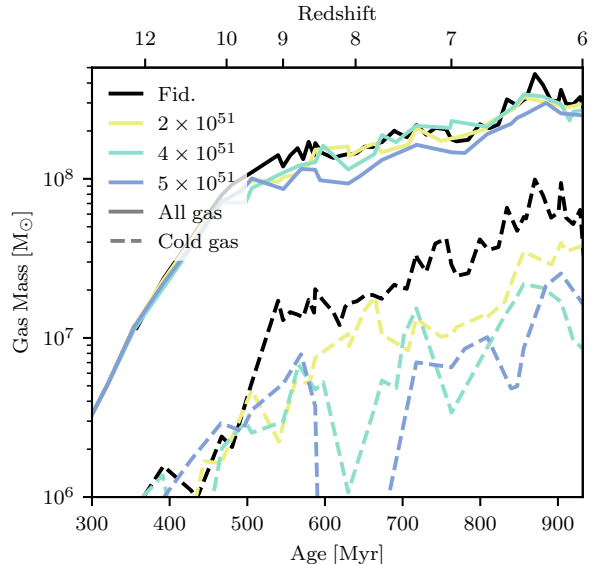


FIG. 9.— Total gas (solid lines) or cold ($T < 500$ K) gas mass (dashed lines) within haloes as a function of redshift for the fiducial model (black) and models with varying SN energies (colors). Increasing feedback energy can diminish the available total and cold gas content in the galaxy, leading to a suppression of the final stellar mass (Figure 7).

value. This is likely due to both ejective and preventative feedback and could explain why the stellar mass growth of the $5 \times$ boost model is fundamentally different from the other simulations. However, between $z \sim 10.5 - 9.5$, right at the time of the first merger, the model with the highest SN energy has temporarily more cold gas than the other boosted models. This provides an explanation as to why there is such a strong upturn in the cumulative stellar mass for the strongest feedback model at these redshifts in Figure 7. The cold gas is then very strongly suppressed for a long duration leading to a decline in the average SFR.

In all model variations, the amount of cold gas is decreased at $z < 10$ compared to the fiducial model which helps explain the decrease in total stellar mass formed. However, because the gas is still within the haloes, continuous energy must be injected in order to prevent the gas from collapsing and forming stars. For a SN boost of $5 \times$, more gas is expelled entirely from the halo compared to the other models, as seen by an overall decrease in total gas mass in Figure 9. For this specific model, up to $\sim 50\%$ of the baryons can be ejected from the halo. Ejective feedback seems to be indicative of regulating star formation for this particular model over a prolonged period of time; although it is difficult to differentiate the role of heating versus ejection or preventative feedback.

Mergers clearly complicate the relationship between SN energy and star formation regulation as do high gas inflow rates. Such a problem is rather unique to the high-redshift Universe where major gas-rich mergers and intense cold gas accretion are more common compared to the low-redshift Universe. For the time periods where the galaxy is evolving more secularly, the feedback energy more directly translates into a stellar mass suppression as seen in other simulations (e.g. Hopkins et al. 2018).

4.5. Feedback Channels

While in Section 4.4 we speculated why the energy per SN may need to be increased at high redshift for both physical and numerical reasons, here we consider two additional forms of feedback that operate on earlier timescales than our fiducial

SN model.

Hypernova Feedback— Stellar evolution models predict that some fraction of low-metallicity massive stars may explode with SN energies of 10 – 40 \times that of a typical SN (Nomoto et al. 2006; Nomoto, Kobayashi & Tominaga 2013). The metal yields from these events are distinct from other evolutionary pathways and thus could provide a unique chemical signature that remains in low-redshift stellar populations and may even be necessary to explain low-redshift chemical abundance patterns in stars (Kobayashi et al. 2006). Recent reionization simulations of Bhagwat et al. (2024) demonstrated how the inclusion of HN¹² regulates star formation, particularly in the low-metallicity regime in the early Universe.

Our model for HN feedback is very similar to Kobayashi, Springel & White (2007). For stars with mass $\geq 20 M_{\odot}$, we assume a mass-energy relation such that a mass of 20, 25, 30, and $> 40 M_{\odot}$ explode with energies of 10, 10, 20, and 40 times that of a typical SN¹³. We also assume that the fraction of stars that explode as HN is strongly dependent on metallicity such that at a metallicity $\leq 5\% Z_{\odot}$, the HN fraction is 50% but at solar metallicity, the HN fraction is 1%.

In the middle panel of the second row of Figure 7, we show the cumulative star formation history of the simulation with HN compared to the fiducial model. By $z = 6$, we find significant regulation such that the total stellar mass is reduced by more than a factor of four. Purely based on energetics, this result is surprising. The mean SN energy in the run with HN is 4.75×10^{51} erg. Despite the lower average energy, the HN model regulates better than any of the models with the uniformly enhanced SN energies, and 30% better than the model with $5\times$ the energy per SN. This result is likely caused by two effects. First, there is clearly a difference between injecting a large amount of energy in a single SN event, as is done in the HN model, and spreading the energy out over multiple events, i.e. impulsivity of the feedback seems to matter. Most similar to this are simulations where realistic time delays are compared with injecting all the SN energy at one particular time (e.g. Kimm et al. 2015; Keller & Kruijssen 2022; Bhagwat et al. 2024). Depending on the exact setup, stellar masses, ISM conditions, and outflow rates can also be affected by a single versus distributed injection of energy. Second, because the HN feedback comes from massive stars, it happens early on in the life-cycle of the star-forming cloud and thus may disrupt the cloud earlier. Considering the results of Section 4.3 where we found little difference in star formation regulation with SN timescale, this latter point may be moot; however, the energy budget may simply be too low with the fiducial SN model to disrupt the dense, high-redshift clouds that form in the fiducial simulation.

The primary issue with the HN model in the context of stellar mass regulation is that it is highly biased towards low-metallicity environments, by construction. While this reflects the fact that HN are not commonly observed in the low-redshift Universe and the chemical abundance patterns of local stars indicate that this process should not occur often at high metallicities (Kobayashi et al. 2006), the halo that we have chosen to model is relatively low mass. Due to the mass-metallicity relation, higher mass haloes tend to be more metal-enriched (e.g. Tremonti et al. 2004) and this relation is now being extended to the very early Universe (e.g. Curti et al. 2024), albeit with significant scatter. Using our model, Choustikov et al. (2025) demonstrated that HN have a clear impact on the mass metallicity relation, particularly at the

low-mass end. Our halo is not generally representative of the results one might find when applying the HN model to a wider sample of galaxy masses. For example, in full box cosmological simulations, Bhagwat et al. (2024) found that HN tend to suppress star formation early on, but as metal enrichment proceeded, significantly less regulation occurred.

This result is however very interesting in the context of our model. Our feedback model is based on that used in Agertz et al. (2013, 2021), where they found that in simulations of Milky Way mass galaxies run to $z = 0$, the galaxies were perfectly consistent with the low-redshift stellar mass-halo mass relation. Since the majority of metals and stars form after $z = 6$ for the Milky Way mass haloes in VINTERGATAN, this early evolution is unlikely to have significant impact on the main galaxy at $z = 0$ ¹⁴. Hence the HN model may provide the extra regulation at high-redshift, without disrupting the expected agreement in the low-redshift Universe. The HN model is not unique in this aspect as really any physical process that suppresses star formation at low metallicity will likely have a similar impact, as long as it does not fundamentally alter subsequent galaxy evolution. However, HN may produce unique chemical signatures in low-metallicity stars that can be observed at $z = 0$.

Ly α Radiation Pressure— Another physical mechanism that preferentially operates at low metallicities is Ly α radiation pressure (Dijkstra & Loeb 2008; Smith, Bromm & Loeb 2017; Kimm et al. 2018; Tomaselli & Ferrara 2021). Energetic photons from young stars ionize their surrounding gas and Ly α photons are subsequently produced predominantly by recombination, but also collisional excitation. To escape the system, the Ly α photons must diffuse both spatially and in frequency. Due to the extreme optical depths that may be present near H II regions, Ly α photons may scatter hundreds (or more) times, imparting momentum into the gas and driving outflows. However, dust can destroy Ly α photons by absorbing them and re-radiating at longer wavelengths. Hence, the presence of dust can significantly reduce the number of scatterings for each Ly α photon. For this reason, Ly α radiation pressure can only operate efficiently at low-metallicity (e.g. Kimm et al. 2018).

The cumulative stellar mass growth normalized by the fiducial model for our run with Ly α radiation pressure is shown in the second row of the middle panel of Figure 7. The stellar mass growth is very similar to the previous model with HN feedback and by $z = 6$, the stellar mass formed in the Lagrange (zoom-in) volume is less than half that of the fiducial model. Should we run the simulation for longer, this model will begin to approach the fiducial run as the increase in metallicity drastically weakens the impact of Ly α radiation pressure.

Ly α radiation pressure operates early on in the star formation cycle as ionizing photons are required to produce significant quantities of Ly α radiation. Furthermore, there is a strong density dependence of the effect as the optical depth is highest in dense gas. We therefore expect that the properties of the ISM is fundamentally different.

In Figure 10, we show the mass-weighted PDFs of gas density, temperature, and oxygen abundance for gas inside of haloes in the redshift interval $6.5 \leq z \leq 8.5$. We compare the fiducial model with the simulations that include HN or Ly α radiation pressure. This redshift interval was chosen to be between the two mergers when the galaxy is more settled to isolate effects outside of starburst periods that may be more generally representative of galaxy formation. Indeed, we find that there is a significant reduction in dense gas in

¹² Note that the HN model of Bhagwat et al. (2024) is different from what is used here although the key principles of a large increase in SN energy and a strong metallicity dependence are present.

¹³ We interpolate energies between these masses.

¹⁴ We emphasize the main galaxy here because early evolution in the epoch of reionization could have profound effects on the satellites.

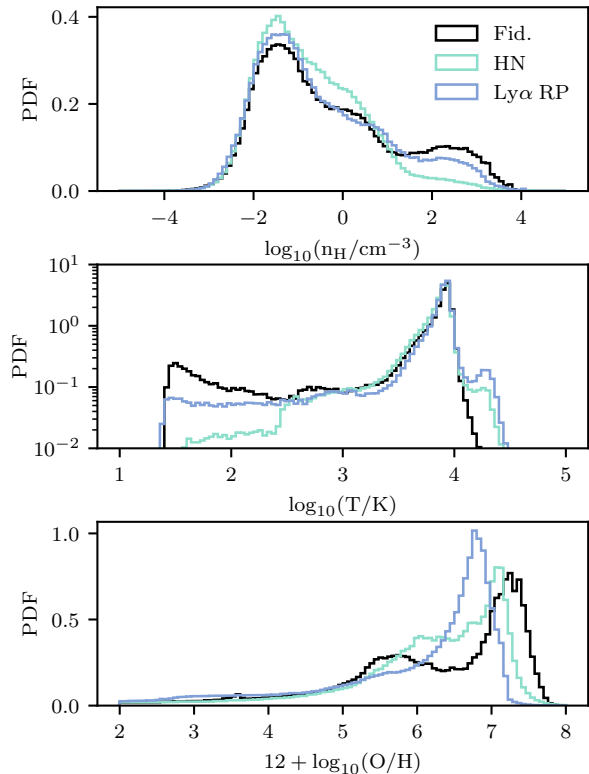


FIG. 10.— Mass-weighted PDFs of gas density (top), gas temperature (middle), and oxygen abundance (bottom) inside haloes in the redshift interval $6.5 \leq z \leq 8.5$. Including additional, strong feedback channels such as supernovae (green) or Ly α radiation pressure (blue) strongly reduces the amount of dense and cold gas, while generating more hot and diffuse gas. This also leads to a suppressed stellar mass (Figure 7).

the runs with HN and Ly α radiation pressure. This is due to two reasons. First, the stronger or additional feedback processes both preferentially operate in dense gas and this is a clear signature of the coupling of the feedback. In the case of Ly α the multiplicative factor for the radiation pressure increases with gas density. With regards to HN, since these only occur for the most massive stars, when they do occur, they will be the first explosions for an individual star particle. We thus empirically find that a HN is more likely to explode in gas with, for example, $n_{\text{H}} > 10^2 \text{ cm}^{-3}$ than a normal SN. Second, because fewer stars have formed in the runs with HN and Ly α radiation pressure, the galaxies are less chemically evolved and metal-line cooling is less efficient which slows the collapse. This is true even though HN inject significantly more O than SNe and the gas fractions are different. PDFs of oxygen abundance are shown in the bottom panel of Figure 10.

Differences are also apparent in the gas temperature distribution. In all three simulations, the warm phase dominates. Consistent with the reduction in high density gas seen for the HN and Ly α radiation pressure models, there is less cold gas in both of these simulations as well compared to the fiducial model. A key difference is that a second peak has emerged in the runs with HN and Ly α radiation pressure that separate the warm neutral medium from the ionized gas. When the dense gas is cleared by the simulations, the Strömgren spheres are much better resolved and more ionized gas emerges in the ISM. This gas does not cool as efficiently as in the case where the Strömgren spheres are unresolved which can help regulate

star formation.

Our results are consistent with that found in the isolated galaxy simulations of Kimm et al. (2018). More specifically, their simulations with SN and Ly α radiation pressure formed fewer stars than their model without Ly α radiation pressure. Likewise, a key signature of the Ly α radiation pressure was that the dense gas clumps which tended to form bound star clusters were often destroyed in the runs with the additional feedback. However, our implementation of Ly α radiation pressure possibly falls on the optimistic side of what one may expect. Because it is generally too expensive to run Monte Carlo radiative transport on-the-fly in galaxy formation simulations (although c.f. Smith et al. 2018 for an alternative approach), we have relied on a subgrid model for Ly α radiation pressure that is based on high-resolution idealized simulations. More specifically, we have adopted a uniform spherical geometry that effectively maximizes the amount of pressure that can be obtained. In gas with a turbulent geometry, Ly α photons may leak before they scatter enough times to have a dynamical effect on the gas. Second, the Ly α emissivity from recombination scales as a power-law with gas temperature such that at lower temperatures, more Ly α is produced. When the Strömgren spheres are not fully resolved, the temperature represents a mixed of the ionized and neutral phases and may be artificially low, which could result in an overestimate of the number of Ly α photons. In principle, this would also impact collisional production of Ly α but this is expected to be subdominant in H II regions and is thus not included in our model. One must also keep in mind that the production of Ly α is related to the input number of ionizing photons. Here we have used STARBURST99 (Leitherer et al. 1999); however other models, e.g. BPASS (Stanway & Eldridge 2018; Eldridge et al. 2017; Eldridge, Izzard & Tout 2008) are known to produce more ionizing photons per stellar mass, while IMF variations can also impact the ionizing photon budget. For this reason, the numerical over-prediction in Ly α may in part be balanced by uncertainties in the input SED.

4.6. Star Formation Algorithm

Our previous model variations have concerned changes to the star particle mass and feedback. We now consider how the star formation algorithm impacts early galaxy formation. Details of the three additional models we consider are listed in Section 2.4, but briefly, the Jeans and Strömgren models adopt star formation efficiencies per free-fall time that scale more strongly with density compared to the fiducial model, while the density-based model employs a fixed density threshold and efficiency.

The right panel of the second row of Figure 7 shows the cumulative stellar mass growth as a function of time normalized by the fiducial model. The final stellar masses at $z = 6$ are relatively independent of these three modifications of the star formation algorithm. Although the tested star formation algorithms are different, these results are consistent with Hopkins et al. (2018) who argue that star formation is feedback-regulated and the final stellar mass should be relatively insensitive to the details of the algorithm as long as stars form at high enough density.

This result is quite interesting because both the densities of star formation and the properties of the ISM are fundamentally different between the models that adopt different star formation algorithms (see also Hopkins, Narayanan & Murray 2013). In Figure 11, we show the PDF of the densities at which star particles form for the three alternative star formation algorithms compared to the fiducial model. The Jeans and Strömgren models have a similar shape to the fiducial model albeit biased towards slightly lower gas densities. This is an inevitability of making the efficiency scale strongly with gas density. In contrast, when applying the density based star

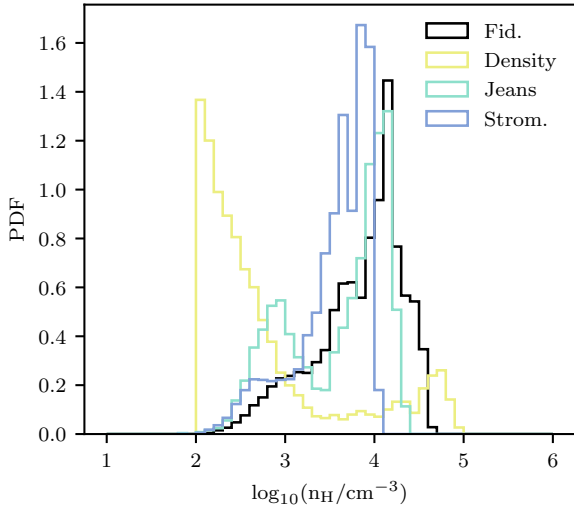


FIG. 11.— PDF of gas densities where stars form. Compared with our fiducial model (black), alternate star formation algorithms lead to large differences in the distribution of star-forming gas and thus the physical conditions of their H II regions.

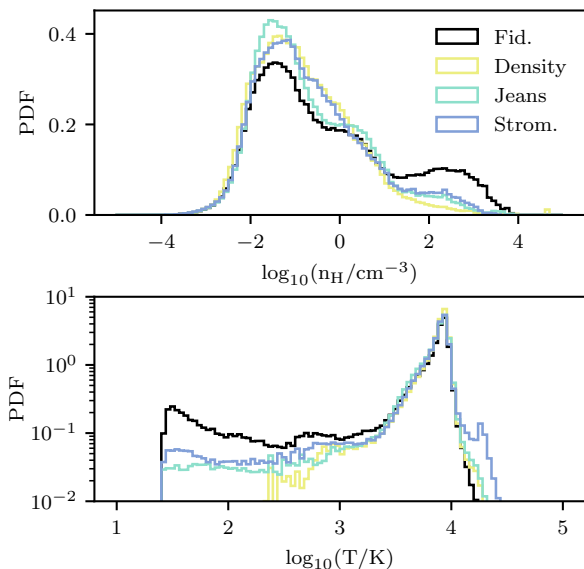


FIG. 12.— Mass-weighted PDFs of gas density (top) and gas temperature (bottom) inside haloes in the redshift interval $6.5 \leq z \leq 8.5$. Despite the small changes in final stellar mass, the ISM structure is fundamentally modified by swapping between our fiducial model (black) and other star formation algorithms (colored lines). This has direct consequences on the resulting observable emission lines of the galaxy (Section 5).

formation model, most stars form near the density threshold that we impose.

Changing the SF algorithm clearly impacts the properties of the ISM. In Figure 12, we show mass-weighted density and temperature PDFs of gas within haloes in the redshift interval $6.5 \leq z \leq 8.5$. The model with a density threshold for star formation has the least amount of high-density gas and almost no cold gas below 500 K because this gas is rapidly turned into stars. Similar, but less severe deficits are also

observed in the Jeans and Strömgen star formation models. These latter two models are quite similar in terms of their ISM properties, except for the fact that the ionized peak is much more prevalent in the Strömgen star formation model compared to the Jeans model (by design). Even though the stars form at much lower density in the density-based star formation model, the Strömgen spheres are still generally unresolved.

Because the density-based star formation is the most fundamentally different to the turbulence-inspired star formation criteria, we consider three additional variations changing (a) the efficiency, (b) the efficiency and the density threshold, and finally (c) the efficiency, the density threshold, and the SN energy. The cumulative stellar mass normalized to the fiducial model is shown in the bottom left panel of Figure 7. Changing the efficiency to 100% and/or increasing the density threshold by a factor of 10 has no impact on the final stellar mass. In contrast, increasing the SN energy by a factor of 5 results in significant regulation, consistent with the results of Section 4.4.

4.7. Resolution

We next study how well our simulation converges with changes to spatial and mass resolution. The bottom middle panel of Figure 7 shows the cumulative stellar mass formed normalized to the fiducial model for two additional simulations with a DM particle mass that is $8\times$ higher or lower than the fiducial model while simultaneously allowing for one more or less level of refinement in the AMR hierarchy. By $z = 6$, the stellar masses are well converged; however, at earlier times there are differences. For example, the onset of star formation is delayed in the low resolution model compared to the fiducial and high-resolution simulations. This is to be expected as halo assembly is delayed with lower DM resolution.

Moreover, for a large fraction of its evolution, the high-resolution simulation exhibits up to $10\times$ lower stellar masses. Given that all stellar masses converge by $z = 6$, we conclude that our model is well converged for haloes with masses $\gtrsim 10^9 M_\odot$, but that there might be more significant uncertainties at lower masses. This aligns with the findings in Rosdahl et al. (2018). With simulations sharing many characteristics to ours, they demonstrated good resolution convergence in terms of the UV luminosity function and stellar mass-halo mass relation of $\gtrsim 10^9 M_\odot$ objects (see also Kang et al. 2024).

4.8. Cooling function and radiative transfer

We consider two final variations to our fiducial model. To mitigate the computational cost of solving radiative transfer, it is typical to adopt a speed of light that is significantly larger than typical gas velocities, but significantly lower than the full value of c (see e.g. Rosdahl et al. 2013). Lowering c to $c_{\text{sim}} < c$ is justified as long as ionization fronts move slowly, which is the case in the higher gas densities close to galaxies, which is the focus of our current study. The situation is different in the IGM where ionization front velocities can be much faster (e.g. Deparis et al. 2019).

However, sub-ionizing radiation fronts (e.g. Lyman-Werner radiation) may be artificially slowed down with a reduced speed of light, as their optical depths are much lower. We thus run an additional simulation adopting $c_{\text{sim}} = 0.1c$, $10\times$ higher than the fiducial model ($c_{\text{sim}} = 0.01c$) to verify convergence against this parameter. The bottom right panel of Figure 7 shows the resulting stellar mass growth that is nearly identical to the fiducial model. Any numerical lag of Lyman-Werner photon fronts do not impact the global stellar mass evolution in our simulations. This is likely because metal line cooling quickly dominates over H_2 cooling at metallicities $\gtrsim 10^{-4} Z_\odot$ (see Figure 1) and that molecular gas is not necessary for star

formation once the system is metal-enriched (e.g. [Glover & Clark 2012](#)). Note that [Pallottini et al. \(2022\)](#) estimated that under certain high-redshift conditions, the photodissociation region fronts move slower than our assumed value of c_{sim} .

In contrast, the exact details of metal cooling may be important for the efficiency of star formation and the initial mass function (e.g. [Safranek-Shrader, Milosavljević & Bromm 2014b](#); [Sharda et al. 2023](#)). To further test the robustness of our results to the choice of metal cooling, we have run a simulation where we replace the non-equilibrium ion-by-ion cooling model in RAMSES-RTZ with the default cooling in RAMSES-RT. The RAMSES-RT model adopts CLOUDY ([Ferland et al. 1998](#)) tables at $T > 10^4$ K that are interpolated over gas density and temperature, assuming scaled solar abundance patterns. At $T < 10^4$ K, the analytic cooling function from [Rosen & Bregman \(1995\)](#) is used.

The bottom right panel of Figure 7 demonstrates that the stellar mass growth in the simulation is reasonably independent of the chosen cooling model. These results again agree with [Hopkins et al. \(2018\)](#), where various simple toy models were adopted to understand the impact of cooling on global galaxy evolution and only small changes were found.

Nevertheless, cooling does have a strong impact on the structure of the ISM. For example, 1D models of [Kim et al. \(2023\)](#) show how the ISM can lose its multi-phase nature under certain assumption regarding the cooling functions. These effects are, to some extent, subdued in 3D in the presence of turbulence, gravitational compression, and various other galaxy formation processes. To visualize these distinctions, Figure 13 shows 2D mass-weighted histograms of gas density and temperature for all gas in the Lagrangian region of the main halo in the redshift interval $6 \leq z \leq 8$. Despite the similarities in final stellar mass, the ISM structure is starkly different between cooling functions. Dense gas in our fiducial model becomes much colder, more rapidly above a density of $\sim 1 \text{ cm}^{-3}$ where thermal instabilities occur. In contrast, the simple cooling model begins efficient cooling at slightly lower densities, but the decrease in temperature is more gradual, consistent with expectations from the 1D calculations of [Kim et al. \(2023\)](#). This clearly demonstrates that the cooling strongly impacts the thermochemistry of the ISM, even if stellar mass is converged. Excitingly, such differences would have an out-sized impact on observable properties such as collisionally excited emission lines where emissivity depends exponentially on gas temperature. We turn next to quantifying how to distinguish models based off their emission line ratios.

5. CONSTRAINING HIGH-REDSHIFT GALAXY FORMATION MODELS WITH ISM OBSERVATIONS

Prior to JWST, constraints on early galaxy formation primary came from photometric data in the rest-frame UV from HST for hundreds of galaxies and ALMA detections of IR emission lines for a handful of objects. The inferred stellar mass-halo mass relation (e.g. [Behroozi, Wechsler & Wu 2013](#); [Behroozi et al. 2019](#); [Moster, Naab & White 2013, 2018](#)) has commonly been used at high redshift; however, there are clear systematic effects, often related to the assumed star formation history model (or prior in the case of a non-parametric model) that lead to > 1 dex uncertainty in stellar masses ([Narayanan et al. 2024](#)). The UV luminosity function represents an alternative (e.g. [Rosdahl et al. 2018](#)), although the bright end is highly sensitive to assumptions on dust. Multiple simulations have been able to reproduce the UV luminosity function, often by calibration, despite fundamental differences in the underlying model (e.g. [Gnedin 2014](#); [Rosdahl et al. 2018](#); [Pawlik et al. 2017](#); [Kannan et al. 2022](#)). With JWST, we can move to much larger samples of galaxies with photometric (in mul-

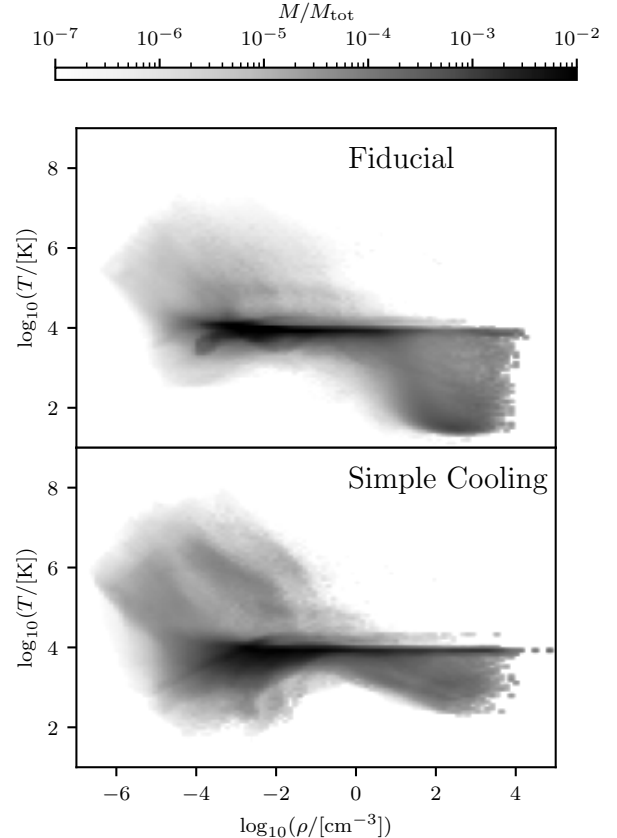


FIG. 13.— 2D mass-weighted histograms of gas density and temperature for all gas in the Lagrange (zoom-in) volume of the main halo between $6 \leq z \leq 8$. Replacing the non-equilibrium cooling of RAMSES-RTZ (top) with an analytic cooling function (bottom) reduces the amount of cold, dense gas, changing the ISM structure, even if the total stellar mass of the galaxy is remains the same (Figure 7).

tiples bands) and spectroscopic data. For example [Katz et al. \(2023b\)](#) showed that matching galaxy colors is significantly more difficult than UV luminosity since the latter is highly dependent on both dust and star formation history. Moreover, seeing redder with JWST compared to HST allows us to extend the baseline of available data deep into the epoch of reionization. Models that may have performed well at $z = 6$ often struggle at $z > 9$ (e.g. [Finkelstein et al. 2023a](#); [Weibel et al. 2024](#)).

The properties of the ISM hold a significant amount of information on the conditions of star formation in the early Universe. For simulations that match the UV luminosity function, they often struggle to reproduce certain emission line luminosity functions (e.g. [Meyer et al. 2024](#)). The vast majority of large cosmological simulations of the early Universe do not model or resolve the detailed properties of the ISM (e.g. [Gnedin 2014](#); [Kannan et al. 2022](#); [Pawlik et al. 2017](#); [Lovell et al. 2021](#)) and the constraining power of the high-redshift ISM via JWST observations is thus a strong motivation for simulations that do reach the required resolutions (e.g. [Rosdahl et al. 2018](#); [Ma et al. 2018](#); [O’Shea et al. 2015](#)). Many of the variations on the fiducial model result in no significant change in stellar mass or star formation rate, but the properties of the ISM are fundamentally different which can have a large impact on observable properties. Here we demonstrate a few examples of how certain models can be ruled in or out

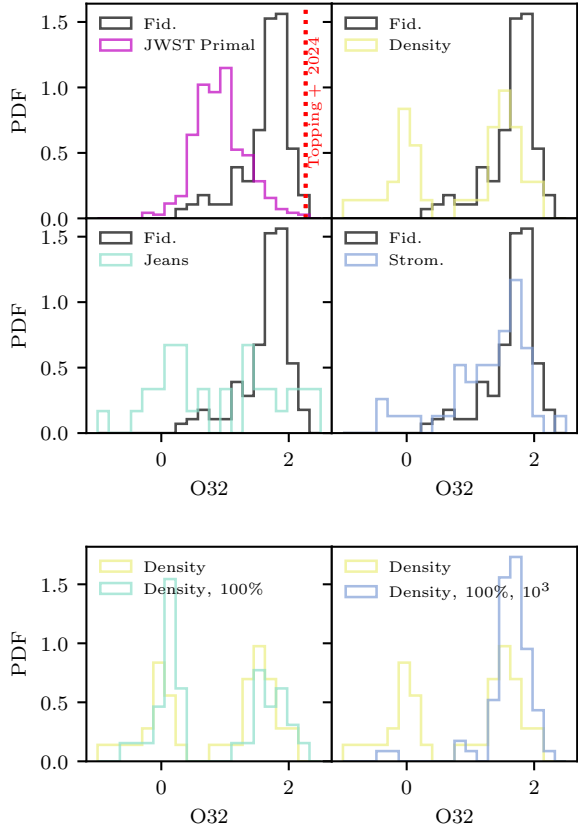


FIG. 14.— PDFs of O32 where we either vary the star formation algorithm (top) or vary the properties of the density-based star formation algorithm by using a higher efficiency or higher gas density threshold (bottom). Swapping algorithms generates shifts in emission line ratios that are larger than the current width of observed data (purple, from Cameron et al. 2023c; Topping et al. 2024b). Even modest changes to input parameters within a given algorithm (e.g. blue vs. green in bottom panel going from 10^2 cm^{-3} to 10^3 cm^{-3} in SF threshold) can have an impact on observables.

with emission lines.

5.1. The O32 diagnostic

Both [O III] $\lambda 5007$ and [O II] $\lambda \lambda 3727$ are readily observable with NIRSspec or a combination of NIRSspec and MIRI at $z \gtrsim 9.5$ (e.g. Bunker et al. 2023; Castellano et al. 2024; Zavala et al. 2024). The O32 ratio (defined as $\log_{10} [\text{O III}] \lambda 5007 / [\text{O II}] \lambda \lambda 3727$) is particularly interesting in the context of our work due to its sensitivity to the ionization parameter (e.g. Kewley, Nicholls & Sutherland 2019). Furthermore, the critical densities of both [O II] lines are smaller than [O III] $\lambda 5007$. In principle, star formation occurring at higher densities and with higher efficiencies would simultaneously boost the ionization parameter and be above the critical density for [O II] emission, leading to higher O32 ratios.

In Figure 14, we show the PDF of O32 values for all uncontaminated haloes in the Lagrange (zoom-in) volume of the main object at all redshifts with $H\alpha$ luminosities $> 10^{39} \text{ erg s}^{-1}$ for the fiducial model. The luminosity cut is applied to ensure that the galaxy is undergoing an active starburst and there are on average 70 galaxies in each PDF. We contrast them with the same objects evolved with different star formation algorithms. The fiducial model (black) tends to form stars at the highest densities and this leads to the highest O32 values. In contrast, the model with the density-

based star formation (yellow) generally exhibits much lower O32 values. The models with the Jeans and the Strömgen star formation algorithms form stars at slightly lower densities than the fiducial model which again shifts O32 to lower values. For comparison, we show high-redshift data from the JWST Primal database (Heintz et al. 2024) in magenta and a galaxy with one of the highest O32 values ever detected at high redshift (Topping et al. 2024b) in red. While our one simulated galaxy is in no way fully representative of the observed galaxy population, it reaches a UV magnitude that is currently accessible by gravitational lensing in both spectroscopic and photometric surveys (e.g. Bezanson et al. 2022; Vanzella et al. 2023; Naidu et al. 2024). Nevertheless, we recognize that our single object and relatively few data points may limit the generalizability of our results especially considering that the $H\alpha$ luminosities and UV magnitudes of galaxies in the JWST Primal database are typically brighter than what we have simulated. However, it is clear from our numerical experiments that observational data can be used to constrain the physical inputs into numerical simulations (should we be able to simulate more massive galaxies) beyond what can be done with integrated stellar masses and UV luminosity functions.

We emphasize that O32 PDF is highly sensitive to even minor variations in the star formation algorithm, and of parameters within a given algorithm. For example, in the bottom panel of Figure 14 we show the PDF of O32 for the density-based star formation algorithm (yellow) where we have either increased the efficiency from 10% to 100% (green) or we have increased the density threshold from 10^2 cm^{-3} to 10^3 cm^{-3} and the efficiency to 100% (blue). The shapes of the PDFs are different in all three cases. More quantitatively, we have run a two-sample KS test comparing the O32 distributions of the modified simulations to the fiducial models and found that the p -values are always less than 0.05. This demonstrates that the ionized gas can also probe the star formation efficiency in a similar way to the molecular gas (Hopkins et al. 2013; Onus, Krumholz & Federrath 2018). Modifying the value of the density threshold, however, leads to a stronger change in O32 compared to increasing the efficiency.

5.2. The C43 diagnostic

Like O32, the ratio of $\log_{10} \text{ C IV } \lambda \lambda 1550 / [\text{C III}] \lambda \lambda 1908$ is also a tracer of ionization parameter. The ionization potential of C^{3+} is 47.9 eV compared to 35.1 eV for O^{++} and hence this ratio traces higher ionization states compared to O32. Being UV lines, C43 can be observed to higher redshift than O32 with NIRSspec. Moreover, some have suggested that C43 is a tracer of LyC escape (Schaerer et al. 2022). In Figure 15 we show PDFs of C43 for the fiducial model compared with variations of the density-based star formation algorithm. While the fiducial model predicts that nearly all star-forming galaxies will have stronger C IV emission, depending on the parameters of the density-based model, either C IV or [C III] can dominate. The trends are very similar to that of O32 although the spread is slightly less pronounced. KS tests again show p -values < 0.05 when comparing the density-based star formation models to the fiducial model.

One possible difference between the ratios of O32 and C43 is how the elements are enriched. Oxygen comes primarily from SN while C is enriched by SN and AGB winds (e.g. Kobayashi, Karakas & Lugaro 2020). For a supernova, the relevant timescale is when the shell cools and begins to re-integrate into the ISM. This timescale scales inversely with gas density¹⁵ (e.g. Thornton et al. 1998; Kim & Ostriker 2015) and is ~ 50 times shorter for a density of 10^5 cm^{-3} compared to 10^2 cm^{-3} . SN will on average explode at higher

¹⁵ The exponent on density is ~ -0.55 .

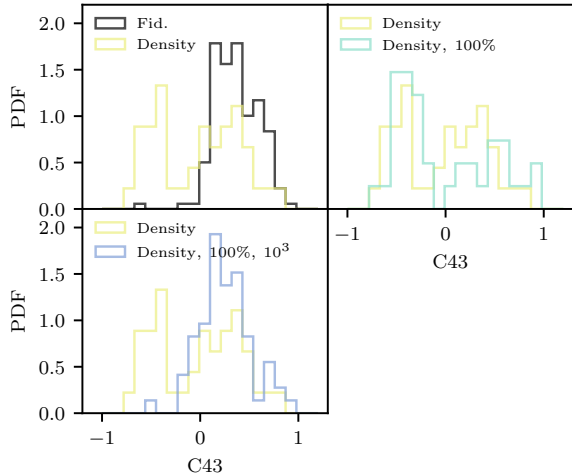


FIG. 15.— Same as Figure 14, but for the C43 line ratio.

densities when a higher density threshold is used for star formation which will lead to the metallic ejecta from SNe being re-illuminated on a shorter timescale. If the timescale is much shorter than the lifetime of a massive star, detecting extremely metal-poor galaxies will become more difficult. In principle, the different density thresholds for star formation will lead to different timescales for this effect, but higher resolution simulations that resolve each SN remnant will be needed to confirm whether this is expected to happen.

5.2.1. The [O III] 4363/5007 diagnostic

While O32 probes ionization parameter and gas density, $\log_{10}[\text{O III}] 4363/5007$ provides insight into gas temperature¹⁶. This ratio has now been observed for numerous high-redshift galaxies (e.g. Katz et al. 2023c; Curti et al. 2023; Laseter et al. 2024; Morishita et al. 2024). Different feedback models can subtly change the temperature of the ISM and because of the strong sensitivity of this metric to gas temperature, it may help discriminate between models.

In Figure 16 we show a PDF of [O III] 4363/5007 for galaxies in the fiducial model compared with models with HN (yellow), Ly α radiation pressure (green), and a $5\times$ boost in the SN energy (blue). In general, the fiducial model has the lowest gas temperatures, followed by the model with Ly α radiation pressure. The highest temperature gas is found in the models with HN and $5\times$ boost in the SN energy. As above, KS tests indicate that these distributions are quantitatively different. There are a few reasons why these differences occur. First the models with HN and a $5\times$ boost in the SN energy simply inject more energy into the ISM and hence the gas temperature can be higher. The effect is less extreme for the Ly α radiation pressure model. Second, the fiducial model is more chemically evolved than the other models and the enhanced metallicity means that the ISM can cool more efficiently. Hence this metric encapsulates both metallicity and energy budget.

For comparison, we show observational data from Morishita et al. (2024) at $z > 6$ for systems where both [O III] lines have been detected. Again, our small zoom simulations cannot be representative of the observed galaxy population, but it is clear that different feedback channels lead to systematically distinct ISM temperatures.

¹⁶ Note that this only true up to gas densities of $\sim 10^5 \text{ cm}^{-3}$ (see e.g. Katz et al. 2023c).

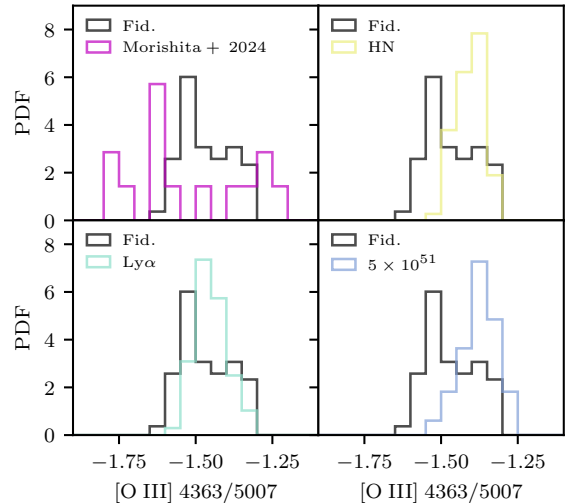


FIG. 16.— [O III] 4363/5007 ratio for our fiducial model (black). This emission line ratio is highly sensitive to the temperature structure of the ISM – boosting the feedback energy with either HN feedback (yellow), Ly α radiation pressure (green), or a $5\times$ boosted SN energy systematically shifts the PDF to higher ratios and thus higher electron temperatures. We also show high-redshift observations from Morishita et al. (2024) in magenta. Note that for a gas density of 500 cm^{-3} , electron temperatures of 10^4 , $10^{4.3}$, and $10^{4.5}$ K correspond to [O III] 4363/5007 ratios of -2.185, -1.475, and -1.217, respectively.

5.3. Discussion on Observational Diagnostics

We have demonstrated that the observable properties of the ISM are sensitive to the detailed implementation of galaxy formation physics. If samples of simulated galaxies can be created that match the selection functions of observed high-redshift galaxies, there is an opportunity to use the observable properties to constrain the input physics and the structure of the ISM in simulations. Here we have focused primarily on emission line ratios from oxygen as they are readily observable at high-redshift and they are less sensitive to the exact details of early chemical enrichment for which there remain significant uncertainties. Nevertheless, other line ratios observable by JWST from C⁺⁺ and N³⁺ probe different gas densities and may help construct a density PDF that will be even more constraining than a single line ratio. Furthermore, the exact chemical abundances are sensitive to enrichment channel and initial mass function and could thus be used to further constrain high-redshift physics. Here we only aimed to demonstrate a few examples of what is now possible. One of the key advantages of RAMSES-RTZ is that it can predict these emission line ratios self-consistently without post-processing, which opens a new avenue to understand early galaxy evolution.

6. CONCLUSIONS

We have introduced a new model (MEGATRON) for cosmological simulations of galaxy formation with on-the-fly multi-frequency radiative transfer and non-equilibrium primordial, molecular, and metal chemistry. Key features of the model are that the thermochemistry is designed to reproduce the conditions of the local ISM at solar metallicity (a probe of neutral gas; Figure 1) and it is consistent with 1D photoionization models used to predict nebular emission lines from H II regions (a probe of ionized gas; Figure 2). Furthermore, star formation is based on turbulent criteria that are designed to mimic results from higher resolution simulations (Federath & Klessen 2012; Padoan & Nordlund 2011), while the

adopted feedback prescription follows a model that has been shown to reproduce many of the properties of Milky Way-like galaxies at $z = 0$ (Agertz et al. 2013; Agertz & Kravtsov 2015; Agertz et al. 2021). We run numerous simulations to understand how the model performs in the context of high-redshift galaxy formation and to changes in the fiducial parameters. Our work focuses on a single halo that reaches a halo mass of $\sim 10^9 M_\odot$ at $z = 6$ with a stellar mass up to $\sim 10^7 M_\odot$, depending on model. By considering the entire history of the halo and uncontaminated neighbours within the Lagrange regions, we analyze ~ 70 galaxies per simulation. Our primary conclusions are as follows:

1. Within the context of our model, numerous parameter choices such as the mass of the star particle, the star formation efficiency per free-fall time, the timescale over which SN explode, resolution, cooling function, and star formation algorithm have little impact on the final stellar mass of the object (Figure 7). Deviations may occur in the star formation history at earlier times when the halo is less massive, but once the halo reaches a mass of $\sim 10^9 M_\odot$, the stellar mass converges. Thus, in high-redshift conditions with significant inflows and mergers, the spatial and temporal clustering of stellar feedback, star formation algorithm, and detailed cooling physics are secondary parameters for star formation regulation, even if they may induce large shifts in gas densities at which stars form and SN explode.
2. The total feedback energy budget is a key parameter that controls the final stellar mass of the halo. Either arbitrarily increasing the SN energy, or accounting for additional feedback channels (e.g. hypernovae, Ly α radiation pressure) both suppress the final stellar mass by reducing the dense, cold gas content of the halo (Figure 9 and 10). Impulsivity also matters, i.e. we find that the HN are more effective at regulating star formation as they inject more energy in a single event compared to simply increasing the energy budget of each SN by a smaller amount. The effect is also non-linear in that a threshold amount of energy must be injected before significant differences in stellar mass are seen. For our simulations, this seems to occur at 5×10^{51} erg per SN.
3. Even if most model variations and parameter choices yield modest changes to the integrated stellar mass, the structure of the ISM is very sensitive to these choices. In particular, the densities of gas surrounding young stars, and the ISM density and temperature PDFs can vary strongly with the choice of star formation algorithm (Figure 12) or the adopted cooling function (Figure 13). These differences modify the distribution function of strong emission line ratios that are particularly sensitive to density and ionization parameter (e.g. O32, C43; Figure 14, 15) and temperature ([O III] 4363/5007; Figure 16). Such line ratios are now observable to $z \gtrsim 10$ with JWST.

Taken together, our results bridge a necessary gap between

high-redshift numerics and the current observational progress following the advent of JWST. Moving forward, ISM observations will represent a new and powerful tool to constrain the detailed physics of galaxy formation simulations, offering a complementary angle to obtain a complete understanding of the ISM and feedback across all cosmic epochs. This work also showcases the power of accounting for non-equilibrium chemistry and radiative transfer in galaxy simulations, paving the way for future simulations of the early Universe using RAMSES-RTZ that can directly be compared to JWST photometric and spectroscopic data.

ACKNOWLEDGMENTS

This work made extensive use of the dp265 and dp016 projects on the DiRAC ecosystem. HK is particularly thankful to Christopher Mountford and Alastair Basden for support on DiAL3 and Cosma8, respectively. HK and MR thank Jonathan Patterson for support with Glamdring. HK thanks Julien Devriendt, Adrianne Slyz, Yohan Dubois, Andrey Kravtsov, and Mark Krumholz for enlightening discussions. The authors thank the referee for their constructive comments.

MR is supported by the Beecroft Fellowship funded by Adrian Beecroft. OA and CC acknowledge support from the Knut and Alice Wallenberg Foundation, the Swedish Research Council (grant 2019-04659), and the Swedish National Space Agency (SNSA Dnr 2023-00164). TK was supported by the National Research Foundation of Korea (NRF) grant funded by the Korea government (No. 2020R1C1C1007079 and No. 2022R1A6A1A03053472). This work used the DiRAC@Durham facility managed by the Institute for Computational Cosmology on behalf of the STFC DiRAC HPC Facility (www.dirac.ac.uk). The equipment was funded by BEIS capital funding via STFC capital grants ST/P002293/1, ST/R002371/1 and ST/S002502/1, Durham University and STFC operations grant ST/R000832/1. This work also used the DiRAC Data Intensive service at Leicester, operated by the University of Leicester IT Services, which forms part of the STFC DiRAC HPC Facility. The equipment was funded by BEIS capital funding via STFC capital grants ST/K000373/1 and ST/R002363/1 and STFC DiRAC Operations grant ST/R001014/1. DiRAC is part of the National e-Infrastructure.

We thank the developers and maintainers of PYNBODY (Pontzen et al. 2013, 2024), NUMPY (van der Walt, Colbert & Varoquaux 2011; Harris et al. 2020), SCIPY (Virtanen et al. 2020), JUPYTER (Ragan-Kelley et al. 2014), MATPLOTLIB (Hunter 2007), the Astrophysics Data Service and the arXiv preprint repository for providing open-source software and services that were used extensively in this work.

The main roles of the authors were, using the CRediT (Contribution Roles Taxonomy) system¹⁷: **Harley Katz: Conceptualization; Data curation; Formal analysis; Investigation; Writing – original draft.** **Martin P. Rey: Conceptualization; Writing – original draft.** **Corentin Cadiou: Conceptualization; Writing – original draft.** **Taysun Kimm: Conceptualization; Investigation; Writing – original draft.** **Oscar Agertz: Conceptualization; Investigation; Writing – original draft.**

REFERENCES

- Agertz O., Kravtsov A. V., 2015, *ApJ*, 804, 18
 Agertz O., Kravtsov A. V., Leitner S. N., Gnedin N. Y., 2013, *ApJ*, 770, 25
 Agertz O. et al., 2020, *MNRAS*, 491, 1656
 Agertz O. et al., 2021, *MNRAS*, 503, 5826
- Agertz O., Teyssier R., Moore B., 2011, *MNRAS*, 410, 1391
 Aldrovandi S. M. V., Pequignot D., 1973, *A&A*, 25, 137
 Anninos P., Zhang Y., Abel T., Norman M. L., 1997, *New A*, 2, 209
 Arnaud M., Raymond J., 1992, *ApJ*, 398, 394
 Arnaud M., Rothenflug R., 1985, *A&AS*, 60, 425
 Baczynski C., Glover S. C. O., Klessen R. S., 2015, *MNRAS*, 454, 380
 Badnell N. R., 2006, *ApJS*, 167, 334

¹⁷ <https://authorservices.wiley.com/author-resources/Journal-Authors/open-access/credit.html>

- Badnell N. R. et al., 2003, *A&A*, 406, 1151
 Bakes E. L. O., Tielens A. G. G. M., 1994, *ApJ*, 427, 822
 Barragán P., Errea L. F., Méndez L., Rabadán I., Riera A., 2006, *ApJ*, 636, 544
 Behroozi P., Wechsler R. H., Hearin A. P., Conroy C., 2019, *MNRAS*, 488, 3143
 Behroozi P. S., Wechsler R. H., Wu H.-Y., 2013, *ApJ*, 762, 109
 Benincasa S. M., Wadsley J., Couchman H. M. P., Keller B. W., 2016, *MNRAS*, 462, 3053
 Benitez-Llambay A., Frenk C., 2020, *MNRAS*, 498, 4887
 Bezanson R. et al., 2022, arXiv e-prints, arXiv:2212.04026
 Bhagwat A., Costa T., Ciardi B., Pakmor R., Garaldi E., 2024, *MNRAS*
 Bialy S., Sternberg A., 2019, *ApJ*, 881, 160
 Black J. H., 1981, *MNRAS*, 197, 553
 Black J. H., Dalgarno A., 1977, *ApJS*, 34, 405
 Blondin J. M., Wright E. B., Borkowski K. J., Reynolds S. P., 1998, *ApJ*, 500, 342
 Bonazzola S., Heyvaerts J., Falgarone E., Perault M., Puget J. L., 1987, *A&A*, 172, 293
 Bovino S., Grassi T., Capelo P. R., Schleicher D. R. G., Banerjee R., 2016, *A&A*, 590, A15
 Bunker A. J. et al., 2023, arXiv e-prints, arXiv:2306.02467
 Burton M. G., Hollenbach D. J., Tielens A. G. G. M., 1990, *ApJ*, 365, 620
 Cameron A. J., Katz H., Rey M. P., Saxena A., 2023a, *MNRAS*, 523, 3516
 Cameron A. J., Katz H., Witten C., Saxena A., Laporte N., Bunker A. J., 2023b, arXiv e-prints, arXiv:2311.02051
 Cameron A. J. et al., 2023c, *A&A*, 677, A115
 Capelo P. R., Bovino S., Lupi A., Schleicher D. R. G., Grassi T., 2018, *MNRAS*, 475, 3283
 Carniani S. et al., 2025, *A&A*, 696, A87
 Carniani S. et al., 2024, arXiv e-prints, arXiv:2405.18485
 Castellano M. et al., 2024, arXiv e-prints, arXiv:2403.10238
 Cen R., 1992, *ApJS*, 78, 341
 Ceverino D., Glover S. C. O., Klessen R. S., 2017, *MNRAS*, 470, 2791
 Charbonnel C., Schaerer D., Prantzos N., Ramírez-Galeano L., Fragos T., Kuruvanthodi A., Marques-Chaves R., Gieles M., 2023, *A&A*, 673, L7
 Chemerynska I. et al., 2023, arXiv e-prints, arXiv:2312.05030
 Chevance M. et al., 2022, *MNRAS*, 509, 272
 Chevance M. et al., 2020, *Space Sci. Rev.*, 216, 50
 Choustikov N. et al., 2025, arXiv e-prints, arXiv:2510.06347
 Commerçon B., Debout V., Teyssier R., 2014, *A&A*, 563, A11
 Curti M. et al., 2023, *MNRAS*, 518, 425
 Curti M. et al., 2024, *A&A*, 684, A75
 Curtis-Lake E. et al., 2023, *Nature Astronomy*, 7, 622
 D'Agostino J. J., Kewley L. J., Groves B., Byler N., Sutherland R. S., Nicholls D., Leitherer C., Stanway E. R., 2019, *ApJ*, 878, 2
 de Graaff A. et al., 2024, arXiv e-prints, arXiv:2404.05683
 Dekel A., Sarkar K. C., Birnboim Y., Mandelker N., Li Z., 2023, *MNRAS*, 523, 3201
 Deng Y., Li H., Kannan R., Smith A., Vogelsberger M., Bryan G. L., 2024a, *MNRAS*, 527, 478
 Deng Y., Li H., Liu B., Kannan R., Smith A., Bryan G. L., 2024b, arXiv e-prints, arXiv:2405.08869
 Deparis N., Aubert D., Ocvirk P., Chardin J., Lewis J., 2019, *A&A*, 622, A142
 Dijkstra M., Loeb A., 2008, *MNRAS*, 391, 457
 Dopita M. A., Kewley L. J., Heisler C. A., Sutherland R. S., 2000, *ApJ*, 542, 224
 Draine B. T., 2011, *Physics of the Interstellar and Intergalactic Medium*
 Draine B. T., Bertoldi F., 1996, *ApJ*, 468, 269
 Dubois Y. et al., 2014, *MNRAS*, 444, 1453
 Efstathiou G., 1992, *MNRAS*, 256, 43P
 Eldridge J. J., Izzard R. G., Tout C. A., 2008, *MNRAS*, 384, 1109
 Eldridge J. J., Stanway E. R., Xiao L., McClelland L. A. S., Taylor G., Ng M., Greis S. M. L., Bray J. C., 2017, *PASA*, 34, e058
 Federrath C., Klessen R. S., 2012, *ApJ*, 761, 156
 Feldmann R. et al., 2025, *MNRAS*, 536, 988
 Feldmann R. et al., 2023, *MNRAS*, 522, 3831
 Ferland G. J. et al., 2017, *Rev. Mexicana Astron. Astrofis.*, 53, 385
 Ferland G. J., Korista K. T., Verner D. A., Ferguson J. W., Kingdon J. B., Verner E. M., 1998, *PASP*, 110, 761
 Ferrara A., Pallottini A., Dayal P., 2023, *MNRAS*, 522, 3986
 Fielding D., Quataert E., Martizzi D., Faucher-Giguère C.-A., 2017, *MNRAS*, 470, L39
 Finkelstein S. L. et al., 2023a, *ApJ*, 946, L13
 Finkelstein S. L. et al., 2023b, arXiv e-prints, arXiv:2311.04279
 Fujimoto S. et al., 2020, *ApJ*, 900, 1
 Galli D., Palla F., 1998, *A&A*, 335, 403
 Gardner J. P. et al., 2023, *PASP*, 135, 068001
 Gardner J. P. et al., 2006, *Space Sci. Rev.*, 123, 485
 Gelli V., Mason C., Hayward C. C., 2024, *ApJ*, 975, 192
 Gentry E. S., Krumholz M. R., Dekel A., Madau P., 2017, *MNRAS*, 465, 2471
 Gentry E. S., Krumholz M. R., Madau P., Lupi A., 2019, *MNRAS*, 483, 3647
 Gentry E. S., Madau P., Krumholz M. R., 2020, *MNRAS*, 492, 1243
 Gerin M. et al., 2015, *A&A*, 573, A30
 Giménez-Arteaga C. et al., 2024, arXiv e-prints, arXiv:2402.17875
 Giménez-Arteaga C. et al., 2023, *ApJ*, 948, 126
 Glazebrook K. et al., 2024, *Nature*, 628, 277
 Glover S. C. O., Abel T., 2008, *MNRAS*, 388, 1627
 Glover S. C. O., Clark P. C., 2012, *MNRAS*, 421, 116
 Glover S. C. O., Federrath C., Mac Low M. M., Klessen R. S., 2010, *MNRAS*, 404, 2
 Gnedin N. Y., 2014, *ApJ*, 793, 29
 Gnedin N. Y., Hollon N., 2012, *ApJS*, 202, 13
 Gnedin N. Y., Tassis K., Kravtsov A. V., 2009, *ApJ*, 697, 55
 Gray W. J., Scannapieco E., Kasen D., 2015, *ApJ*, 801, 107
 Grevesse N., Asplund M., Sauval A. J., Scott P., 2010, *Ap&SS*, 328, 179
 Grisdale K., Agertz O., Renaud F., Romeo A. B., 2018, *MNRAS*, 479, 3167
 Guillet T., Teyssier R., 2011, *Journal of Computational Physics*, 230, 4756
 Haardt F., Madau P., 2012, *ApJ*, 746, 125
 Haiman Z., Thoul A. A., Loeb A., 1996, *ApJ*, 464, 523
 Harikane Y., Nakajima K., Ouchi M., Umeda H., Isobe Y., Ono Y., Xu Y., Zhang Y., 2024, *ApJ*, 960, 56
 Harikane Y. et al., 2020, *ApJ*, 896, 93
 Harris C. R. et al., 2020, *Nature*, 585, 357
 Hashimoto T. et al., 2018, *Nature*, 557, 392
 Heays A. N., Bosman A. D., van Dishoeck E. F., 2017, *A&A*, 602, A105
 Heger A., Woosley S. E., 2002, *ApJ*, 567, 532
 Heintz K. E. et al., 2024, arXiv e-prints, arXiv:2404.02211
 Herrera-Camus R. et al., 2017, *ApJ*, 835, 201
 Hislop J. M., Naab T., Steinwandel U. P., Lahén N., Irododou D., Johansson P. H., Walch S., 2022, *MNRAS*, 509, 5938
 Hollenbach D., McKee C. F., 1979, *ApJS*, 41, 555
 Hollenbach D., McKee C. F., 1989, *ApJ*, 342, 306
 Hopkins P. F., Kereš D., Oñorbe J., Faucher-Giguère C.-A., Quataert E., Murray N., Bullock J. S., 2014, *MNRAS*, 445, 581
 Hopkins P. F., Narayanan D., Murray N., 2013, *MNRAS*, 432, 2647
 Hopkins P. F., Narayanan D., Murray N., Quataert E., 2013, *MNRAS*, 433, 69
 Hopkins P. F. et al., 2018, *MNRAS*, 477, 1578
 Hu C.-Y., Naab T., Walch S., Glover S. C. O., Clark P. C., 2016, *MNRAS*, 458, 3528
 Hu Z., Wibking B. D., Krumholz M. R., Federrath C., 2024, arXiv e-prints, arXiv:2406.11155
 Hui L., Gnedin N. Y., 1997, *MNRAS*, 292, 27
 Hunter J. D., 2007, *Computing in Science and Engineering*, 9, 90
 Isobe Y., Ouchi M., Nakajima K., Harikane Y., Ono Y., Xu Y., Zhang Y., Umeda H., 2023a, *ApJ*, 956, 139
 Isobe Y. et al., 2023b, *ApJ*, 959, 100
 Jeffreson S. M. R., Semenov V. A., Krumholz M. R., 2024, *MNRAS*, 527, 7093
 Jenkins E. B., Tripp T. M., 2011, *ApJ*, 734, 65
 Jin Y., Kewley L. J., Sutherland R. S., 2022, *ApJ*, 934, L8
 Kang C., Kimm T., Han D., Katz H., Devriendt J., Slyz A., Teyssier R., 2024, arXiv e-prints, arXiv:2407.12090
 Kannan R., Garaldi E., Smith A., Pakmor R., Springel V., Vogelsberger M., Hernquist L., 2022, *MNRAS*, 511, 4005
 Katz H., 2022, *MNRAS*, 512, 348
 Katz H. et al., 2024a, arXiv e-prints, arXiv:2408.03189
 Katz H., Ji A. P., Telford G., Shenchna P., 2024b, *The Open Journal of Astrophysics*, 7, 106
 Katz H., Kimm T., Ellis R. S., Devriendt J., Slyz A., 2023a, *MNRAS*, 524, 351
 Katz H., Kimm T., Sijacki D., Haehnelt M. G., 2017, *MNRAS*, 468, 4831
 Katz H. et al., 2022, arXiv e-prints, arXiv:2211.04626
 Katz H. et al., 2020, *MNRAS*, 494, 2200
 Katz H. et al., 2023b, *The Open Journal of Astrophysics*, 6, 44
 Katz H. et al., 2023c, *MNRAS*, 518, 592
 Katz N., 1992, *ApJ*, 391, 502
 Keller B. W., Kruijssen J. M. D., 2022, *MNRAS*, 512, 199
 Keller B. W., Kruijssen J. M. D., Chevance M., 2022, *MNRAS*, 514, 5355
 Keller B. W., Wadsley J., Benincasa S. M., Couchman H. M. P., 2014, *MNRAS*, 442, 3013
 Kennicutt R. C., Evans N. J., 2012, *ARA&A*, 50, 531

- Kewley L. J., Nicholls D. C., Sutherland R. S., 2019, *ARA&A*, 57, 511
- Kim C.-G., Ostriker E. C., 2015, *ApJ*, 802, 99
- Kim C.-G., Ostriker E. C., Raileanu R., 2017, *ApJ*, 834, 25
- Kim J.-G., Gong M., Kim C.-G., Ostriker E. C., 2023, *ApJS*, 264, 10
- Kimm T., Cen R., 2014, *ApJ*, 788, 121
- Kimm T., Cen R., Devriendt J., Dubois Y., Slyz A., 2015, *MNRAS*, 451, 2900
- Kimm T., Haehnelt M., Blaizot J., Katz H., Michel-Dansac L., Garel T., Rosdahl J., Teyssier R., 2018, *MNRAS*, 475, 4617
- Kimm T., Katz H., Haehnelt M., Rosdahl J., Devriendt J., Slyz A., 2017, *MNRAS*, 466, 4826
- Kingdon J. B., Ferland G. J., 1996, *ApJS*, 106, 205
- Kobayashi C., Karakas A. I., Lugaro M., 2020, *ApJ*, 900, 179
- Kobayashi C., Springel V., White S. D. M., 2007, *MNRAS*, 376, 1465
- Kobayashi C., Umeda H., Nomoto K., Tominaga N., Ohkubo T., 2006, *ApJ*, 653, 1145
- Koyama H., Inutsuka S.-I., 2000, *ApJ*, 532, 980
- Kravtsov A., Belokurov V., 2024, arXiv e-prints, arXiv:2405.04578
- Krujssens J. M. D. et al., 2019, *Nature*, 569, 519
- Kulkarni G., Keating L. C., Haehnelt M. G., Bosman S. E. I., Puchwein E., Chardin J., Aubert D., 2019, *MNRAS*, 485, L24
- Lao B.-X., Smith A., 2020, *MNRAS*, 497, 3925
- Laseter I. H. et al., 2024, *A&A*, 681, A70
- Leitherer C. et al., 1999, *ApJS*, 123, 3
- Leung G. C. K. et al., 2023, *ApJ*, 954, L46
- Levermore C. D., 1984, *J. Quant. Spec. Radiat. Transf.*, 31, 149
- Limongi M., Chieffi A., 2018, *ApJS*, 237, 13
- Lovell C. C., Vijayan A. P., Thomas P. A., Wilkins S. M., Barnes D. J., Irodotou D., Roper W., 2021, *MNRAS*, 500, 2127
- Lupi A., Pallottini A., Ferrara A., Bovino S., Carniani S., Vallini L., 2020, *MNRAS*, 496, 5160
- Luridiana V., Morisset C., Shaw R. A., 2015, *A&A*, 573, A42
- Ma X. et al., 2018, *MNRAS*, 478, 1694
- Maoz D., Graur O., 2017, *ApJ*, 848, 25
- Marques-Chaves R. et al., 2024, *A&A*, 681, A30
- Mason C. A., Trenti M., Treu T., 2023, *MNRAS*, 521, 497
- McElroy D., Walsh C., Markwick A. J., Cordiner M. A., Smith K., Millar T. J., 2013, *A&A*, 550, A36
- McKee C. F., Storey J. W. V., Watson D. M., Green S., 1982, *ApJ*, 259, 647
- Meyer R. A. et al., 2024, arXiv e-prints, arXiv:2405.05111
- Morishita T. et al., 2024, arXiv e-prints, arXiv:2402.14084
- Moseley E. R., Draine B. T., Tomida K., Stone J. M., 2021, *MNRAS*, 500, 3290
- Moster B. P., Naab T., White S. D. M., 2013, *MNRAS*, 428, 3121
- Moster B. P., Naab T., White S. D. M., 2018, *MNRAS*, 477, 1822
- Naidu R. P. et al., 2024, arXiv e-prints
- Narayanan D. et al., 2024, *ApJ*, 961, 73
- Nebrin O., Smith A., Lorinc K., Hörnquist J., Larson A., Mellema G., Giri S. K., 2025, *MNRAS*, 537, 1646
- Nelson R. P., Langer W. D., 1997, *ApJ*, 482, 796
- Nomoto K., Kobayashi C., Tominaga N., 2013, *ARA&A*, 51, 457
- Nomoto K., Tominaga N., Umeda H., Kobayashi C., Maeda K., 2006, *Nucl. Phys. A*, 777, 424
- Ocvirk P. et al., 2020, *MNRAS*, 496, 4087
- Oesch P. A. et al., 2016, *ApJ*, 819, 129
- Omukai K., Tsuribe T., Schneider R., Ferrara A., 2005, *ApJ*, 626, 627
- Onus A., Krumholz M. R., Federrath C., 2018, *MNRAS*, 479, 1702
- Oppenheimer B. D., Schaye J., Crain R. A., Werk J. K., Richings A. J., 2018, *MNRAS*, 481, 835
- O'Shea B. W., Wise J. H., Xu H., Norman M. L., 2015, *ApJ*, 807, L12
- Osterbrock D. E., Ferland G. J., 2006, *Astrophysics of gaseous nebulae and active galactic nuclei*
- Padoan P., Nordlund Å., 2011, *ApJ*, 730, 40
- Pallottini A. et al., 2022, *MNRAS*, 513, 5621
- Pawlik A. H., Rahmati A., Schaye J., Jeon M., Dalla Vecchia C., 2017, *MNRAS*, 466, 960
- Pawlik A. H., Schaye J., 2008, *MNRAS*, 389, 651
- Pecaut M. J., Mamajek E. E., 2013, *ApJS*, 208, 9
- Pillepich A. et al., 2018, *MNRAS*, 473, 4077
- Planck Collaboration et al., 2020, *A&A*, 641, A6
- Pontzen A., Cadiou C., svstopyra, nroth0815, Rey M. P., rc-softdev-admin, 2024, pynbody/genetIC: Version 1.5.0
- Pontzen A., Roškar R., Stinson G., Woods R., 2013, pynbody: N-Body/SPH analysis for python. Astrophysics Source Code Library, record ascl:1305.002
- Prgomet M., Rey M. P., Andersson E. P., Segovia Otero A., Agertz O., Renaud F., Pontzen A., Read J. I., 2022, *MNRAS*, 513, 2326
- Ragan-Kelley M., Perez F., Granger B., Kluyver T., Ivanov P., Frederic J., Bussonnier M., 2014, in *AGU Fall Meeting Abstracts*, Vol. 2014, pp. H44D-07
- Rasera Y., Teyssier R., 2006, *A&A*, 445, 1
- Read J. I., Iorio G., Agertz O., Fraternali F., 2017, *MNRAS*, 467, 2019
- Rémy-Ruyer A. et al., 2014, *A&A*, 563, A31
- Renaud F., Agertz O., Andersson E. P., Read J. I., Ryde N., Bensby T., Rey M. P., Feuillet D. K., 2021a, *MNRAS*, 503, 5868
- Renaud F., Agertz O., Read J. I., Ryde N., Andersson E. P., Bensby T., Rey M. P., Feuillet D. K., 2021b, *MNRAS*, 503, 5846
- Renaud F., Segovia Otero Á., Agertz O., 2022, *MNRAS*, 516, 4922
- Rey M. P. et al., 2023, *MNRAS*, 521, 995
- Rey M. P., Pontzen A., Agertz O., Orkney M. D. A., Read J. I., Rosdahl J., 2020, *MNRAS*, 497, 1508
- Richings A. J., Faucher-Giguère C.-A., Gurvich A. B., Schaye J., Hayward C. C., 2022, *MNRAS*, 517, 1557
- Ritter C., Herwig F., Jones S., Pignatari M., Fryer C., Hirschi R., 2018, *MNRAS*, 480, 538
- Rodríguez Montero F., Martín-Alvarez S., Slyz A., Devriendt J., Dubois Y., Sijacki D., 2024, *MNRAS*, 530, 3617
- Röllig M., Ossenkopf V., Jeyakumar S., Stutzki J., Sternberg A., 2006, *A&A*, 451, 917
- Rosdahl J., Blaizot J., 2012, *MNRAS*, 423, 344
- Rosdahl J., Blaizot J., Aubert D., Stranex T., Teyssier R., 2013, *MNRAS*, 436, 2188
- Rosdahl J. et al., 2018, *MNRAS*, 479, 994
- Rosdahl J., Schaye J., Teyssier R., Agertz O., 2015, *MNRAS*, 451, 34
- Rosdahl J., Teyssier R., 2015, *MNRAS*, 449, 4380
- Rosen A., Bregman J. N., 1995, *ApJ*, 440, 634
- Safraneck-Shrader C., Milosavljević M., Bromm V., 2014a, *MNRAS*, 438, 1669
- Safraneck-Shrader C., Milosavljević M., Bromm V., 2014b, *MNRAS*, 438, 1669
- Sanders R. L., Shapley A. E., Topping M. W., Reddy N. A., Brammer G. B., 2023, *ApJ*, 955, 54
- Schaerer D., 2002, *A&A*, 382, 28
- Schaerer D. et al., 2022, *A&A*, 658, L11
- Schaerer D., Meynet G., Maeder A., Schaller G., 1993, *A&AS*, 98, 523
- Schaye J. et al., 2015, *MNRAS*, 446, 521
- Schouws S. et al., 2025, *ApJ*, 988, 19
- Segovia Otero Á., Renaud F., Agertz O., 2022, *MNRAS*, 516, 2272
- Seitenzahl I. R. et al., 2013, *MNRAS*, 429, 1156
- Semenov V. A., 2024, arXiv e-prints, arXiv:2410.23339
- Semenov V. A., Kravtsov A. V., Gnedin N. Y., 2021, *ApJ*, 918, 13
- Senchyna P., Plat A., Stark D. P., Rudie G. C., Berg D., Charlot S., James B. L., Mingozzi M., 2024, *ApJ*, 966, 92
- Sharda P., Amarsi A. M., Grasha K., Krumholz M. R., Yong D., Chiaki G., Roy A., Nordlander T., 2023, *MNRAS*, 518, 3985
- Shen X. et al., 2025, *MNRAS*
- Shen X., Vogelsberger M., Boylan-Kolchin M., Tacchella S., Kannan R., 2023, *MNRAS*, 525, 3254
- Shull J. M., van Steenberg M., 1982, *ApJS*, 48, 95
- Smith A., Bromm V., Loeb A., 2017, *MNRAS*, 464, 2963
- Smith A. et al., 2022, *MNRAS*, 517, 1
- Smith A., Tsang B. T. H., Bromm V., Milosavljević M., 2018, *MNRAS*, 479, 2065
- Smith M. C., Bryan G. L., Somerville R. S., Hu C.-Y., Teyssier R., Burkhardt B., Hernquist L., 2021, *MNRAS*, 506, 3882
- Snaith O. N., Park C., Kim J., Rosdahl J., 2018, *MNRAS*, 477, 983
- Stancil P. C., Schultz D. R., Kimura M., Gu J. P., Hirsch G., Buenker R. J., 1999, *A&AS*, 140, 225
- Stanway E. R., Eldridge J. J., 2018, *MNRAS*, 479, 75
- Steinwandel U. P., Moster B. P., Naab T., Hu C.-Y., Walch S., 2020, *MNRAS*, 495, 1035
- Sternberg A., Dalgarno A., 1989, *ApJ*, 338, 197
- Strömgren B., 1939, *ApJ*, 89, 526
- Sukhbold T., Ertl T., Woosley S. E., Brown J. M., Janka H. T., 2016, *ApJ*, 821, 38
- Sun G., Faucher-Giguère C.-A., Hayward C. C., Shen X., Wetzel A., Cochrane R. K., 2023, *ApJ*, 955, L35
- Teyssier R., 2002, *A&A*, 385, 337
- Thornton K., Gaudlitz M., Janka H. T., Steinmetz M., 1998, *ApJ*, 500, 95
- Tomaselli G. M., Ferrara A., 2021, *MNRAS*, 504, 89
- Topping M. W. et al., 2024a, arXiv e-prints, arXiv:2407.19009
- Topping M. W. et al., 2024b, *MNRAS*, 529, 3301
- Toro E. F., 2009, *Riemann Solvers and Numerical Methods for Fluid Dynamics: A Practical Introduction*, 3rd edn. Springer, Berlin

- Trebitsch M. et al., 2021, *A&A*, 653, A154
Tremonti C. A. et al., 2004, *ApJ*, 613, 898
Umeda H., Nomoto K., 2002, *ApJ*, 565, 385
van der Walt S., Colbert S. C., Varoquaux G., 2011, *Computing in Science and Engineering*, 13, 22
van Leer B., 1979, *Journal of Computational Physics*, 32, 101
Vanzella E. et al., 2023, *A&A*, 678, A173
Verner D. A., Ferland G. J., Korista K. T., Yakovlev D. G., 1996, *ApJ*, 465, 487
Virtanen P. et al., 2020, *Nature Methods*, 17, 261
Voronov G. S., 1997, *Atomic Data and Nuclear Data Tables*, 65, 1
Wang B. et al., 2023, *ApJ*, 957, L34
Weibel A. et al., 2024, *MNRAS*, 533, 1808
Weingartner J. C., Draine B. T., 2001, *ApJ*, 563, 842
Welty D. E., Lauroesch J. T., Wong T., York D. G., 2016, *ApJ*, 821, 118
Willott C. J. et al., 2023, arXiv e-prints, arXiv:2311.12234
Wise J. H., Abel T., Turk M. J., Norman M. L., Smith B. D., 2012, *MNRAS*, 427, 311
Wolfire M. G., Hollenbach D., McKee C. F., Tielens A. G. G. M., Bakes E. L. O., 1995, *ApJ*, 443, 152
Wolfire M. G., McKee C. F., Hollenbach D., Tielens A. G. G. M., 2003, *ApJ*, 587, 278
Yadav N., Mukherjee D., Sharma P., Nath B. B., 2017, *MNRAS*, 465, 1720
Yung L. Y. A., Somerville R. S., Finkelstein S. L., Wilkins S. M., Gardner J. P., 2024, *MNRAS*, 527, 5929
Zavala J. A. et al., 2024, arXiv e-prints, arXiv:2403.10491
Zubko V., Dwek E., Arendt R. G., 2004, *ApJS*, 152, 211

This paper was built using the Open Journal of Astrophysics L^AT_EX template. The OJA is a journal which provides fast and easy peer review for new papers in the `astro-ph`

section of the arXiv, making the reviewing process simpler for authors and referees alike. Learn more at <http://astro.theoj.org>.